OXFORD

Journal of Petrology, 2026, **67**, egag009
https://doi.org/10.1093/petrology/egag009
ADVANCE ACCESS PUBLICATION DATE 3 FEBRUARY 2026
Original Manuscript

Decoding Reservoir Interactions and Pre-Eruptive Timescales: Olivine Insights into the Cracked Mountain Eruption, Mount Meager Volcanic Complex, Canada

SARAH M. AUFRÈRE[1], GLYN WILLIAMS-JONES[1], SÉVERINE MOUNE[2], JAMES K. RUSSELL[3], YANNICK LE MOIGNE[1,4], NATHALIE VIGOUROUX[1,5] and DANIEL J. MORGAN[6]

[1]Centre for Natural Hazards Research, Department of Earth Sciences, Simon Fraser University, 8888 University Drive, Burnaby, BC V5A 1S6, Canada
[2]Laboratoire Magmas et Volcans, CNRS-OPGC-IRD, Université Clermont Auvergne, Campus Universitaire des Cézeaux, 6 Avenue Blaise Pascal, Aubière 63170, France
[3]Department of Earth, Ocean and Atmospheric Sciences, Volcanology and Petrology Laboratory, University of British Columbia, 2207 Main Mall #2020, Vancouver, BC V6T 1Z4, Canada
[4]Natural Resources Canada, Geological Survey of Canada, 605 Robson St Suite 1500, Vancouver, BC V6B 5J3, Canada
[5]Department of Earth and Environmental Sciences, Douglas College, 700 Royal Avenue, New Westminster, BC V3M 5Z5, Canada
[6]School of Earth and Environment, University of Leeds, Woodhouse, Leeds LS2 9JT, UK
*Corresponding author: E-mail: s.aufrere@lancaster.ac.uk
†Handling Editor: Prof. Valentin Troll

Geochemical and textural analyses of 236 olivine phenocrysts reveal the dynamic magmatic processes that shaped the Cracked Mountain eruption (401 ± 38 ka), a glaciovolcanic event within the Mount Meager Volcanic Complex (Garibaldi Volcanic Belt, British Columbia, Canada). This study characterises the magmatic reservoirs involved, their interactions, and key processes such as magma recharge, mixing, storage, and eruption triggering. Two main populations of olivine crystals (Groups 1 and 2), distinguished by their compositions, zoning patterns, and inclusions, reveal interactions between two distinct storage zones prior to the eruption. The deeper reservoir, storing an olivine–plagioclase–augite (OPA)-bearing magma at ~8 km depth (~240 MPa), hosted Group 2 olivine phenocrysts (core compositions $Fo_{79–81}$) with abundant spinel inclusions and no sulphides. At shallower depths (~5 km, ~160 MPa), an olivine–plagioclase (OP) reservoir hosted Group 1 olivine phenocrysts (core compositions $Fo_{\sim 83}$), which lack spinel inclusions but contain rare sulphides. The two magmas subsequently ascended, mixed, and stalled in a shallow reservoir, where skeletal Group 3 phenocrysts ($Fo_{77–78}$) crystallised. Group 1 crystals, once entrained, developed pronounced normal zoning as they equilibrated with the more evolved mixed melt, while Group 2 displayed faint normal zoning due to minimal fractional crystallisation of their host melt (both populations exhibiting overlapping rim compositions within the $Fo_{76–79}$ range). Diffusion modelling of olivine zoning, conducted on 160 profiles, indicates that this mixing occurred within a year of the eruption. Lastly, a late-stage episode of mixing and/or melt oxidation, evidenced by faint Fo reverse zoning, may have destabilised the system and triggered the eruption.

Key words: olivine; diffusion chronometry; basalt; Cascades Volcanic Arc; Garibaldi Volcanic Belt; Mount Meager Volcanic Complex

Introduction

Forecasting the timing of volcanic eruptions remains a significant challenge, particularly for volcanoes lacking comprehensive monitoring systems. For example, many eruptions occurred long before the establishment of modern networks, leaving gaps in our understanding of the processes that precede eruptions. Even today, volcanic monitoring of regions such as the Canadian part of the Garibaldi Volcanic Belt (GVB; the northern extent of the Cascades Volcanic Arc; Fig. 1a) is still in its early stages, with regular satellite remote sensing only recently introduced (Rotheram-Clarke *et al.*, 2023). In the absence of robust monitoring networks prior to an eruption, diffusion chronometry can provide a unique opportunity to reconstruct magmatic timescales. By modelling chemical zoning in minerals found in quenched volcanic deposits, this technique can constrain the relative timing and timescales of various magmatic processes (Chakraborty & Dohmen, 2022) and is not limited by the eruption's age. Diffusion chronometry becomes particularly powerful when combined with monitoring datasets, as it bridges geochemical insights with signals of unrest, thereby improving interpretations of monitoring data (Lynn *et al.*, 2024). To date, olivine crystals are strong candidates for the application of diffusion chronometry because diffusion rates for key elements in olivine (e.g. Fe-Mg, Ni, Ca, and Mn) are well constrained (Chakraborty, 2010).

The Canadian GVB volcanoes remain relatively understudied compared to their US counterparts (Hildreth, 2007; Wieser *et al.*, 2023), largely due to their remoteness and difficulty of access. Of these, the Mount Meager Volcanic Complex (MMVC; *Q̓wel̓q̓welústen* in the Líl̓wat language) has the second highest threat ranking of Canadian volcanoes (Kelman & Wilson, 2024)—mainly attributed to its 2360 years ^{14}C BP, sub-Plinian eruption of volcanic explosivity index 4 (VEI; Newhall & Self, 1982) (Stasiuk *et al.*, 1996; Hickson *et al.*, 1999; Michol *et al.*, 2008; Andrews *et al.*, 2014) and ongoing fumarolic activity (Clance *et al.*, 2024; Unnsteinsson *et al.*, 2024)—and is an ideal site to apply diffusion chronometry. Indeed, the MMVC includes several olivine–phyric mafic eruptions

RECEIVED MARCH 5, 2025; **REVISED** JANUARY 23, 2026; **ACCEPTED** JANUARY 27, 2026

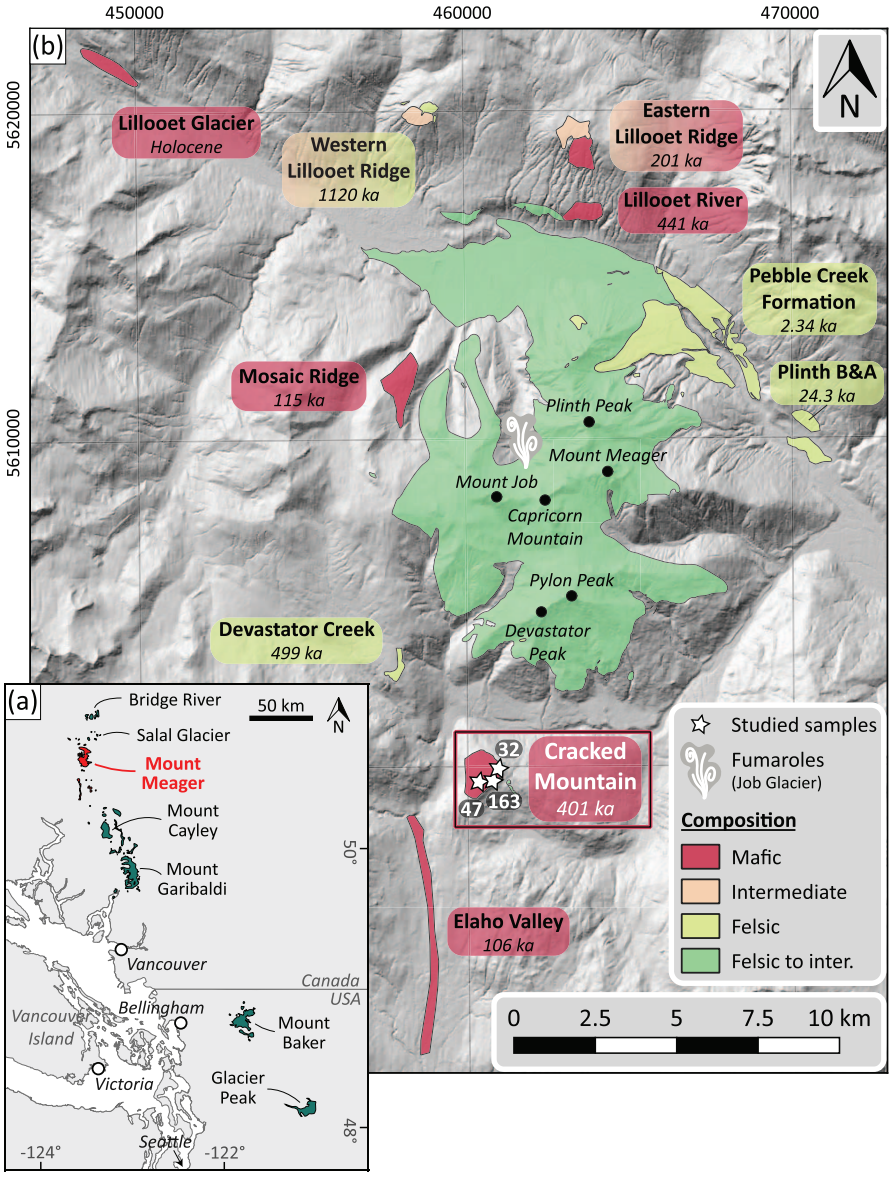

Figure 1. (a) Map showing the volcanic complexes of the GVB, which stretches from Bridge River in British Columbia, Canada to Glacier Peak in Washington, USA (Hildreth, 2007). The MMVC is highlighted in red. (b) Geological map of the MMVC adapted from Aufrère *et al.* (2024) (see references therein) for the CM eruption. Location of the *AW-15-163*, *MH-19-032*, and *MH-19-047* samples studied here are shown by white stars. Coordinate system: UTM Projection Zone 10 N (metres); WGS84 Datum.

spanning the Holocene to ~400 ka, distributed around the Mount Meager massif (Fig. 1b). Furthermore, some of these eruptions are glaciovolcanic in nature, providing quenched deposits such as pillow lavas (Wilson & Russell, 2017, 2019; Harris *et al.*, 2022). Among these glaciovolcanic eruptions, two—namely, the *Lillooet Glacier* and *Cracked Mountain* eruptions (Fig. 1b)—have been the subject of thorough mapping, detailed petrography and geochemical analyses, and thermodynamic modelling to constrain pre-eruptive conditions (Wilson & Russell, 2017; Harris & Russell, 2022). Building on previous work on the *Lillooet Glacier* eruption (Aufrère *et al.*, 2024), this study thus focuses on olivine crystals from the *Cracked Mountain* (CM) eruption (Fig. 1b). We use data collected on 236 olivine phenocrysts (term here used in the descriptive and non-genetic original sense of Iddings, 1892, i.e. crystals visible without magnification) to further constrain pre-eruptive conditions and timescales, characterise magmatic reservoirs and their interactions, and investigate processes including magma mixing, storage, and eruption triggering. These findings contribute to a broader understanding of the MMVC and underscore the utility of olivine in the deciphering of complex magmatic histories.

Cracked Mountain

Cracked Mountain volcano, named for its network of extensional cracks 0.5–20 m wide and up to 30 m deep (Harris *et al.*, 2022), is located southwest of the Mount Meager massif (Fig. 1b). Based on its stratigraphy and paleomagnetic dating, Harris *et al.* (2022) found CM to be monogenetic, with a $^{40}Ar/^{39}Ar$ age of 401 ± 38 ka. CM features steep margins with a local relief of ~250 m and a summit at 1650 m above sea level. It is classified as a transitional tephra-dominated tuya that formed during a sustained eruption within an englacial lake and resulted in the eruption of 0.18 km^3 of sub-alkaline and basaltic (Fig. 2) lapilli tuff, breccia, peperite, pillow and sheet lava, and dykes (Wilson & Russell, 2019; Harris *et al.*, 2022). It thus represents an important geological

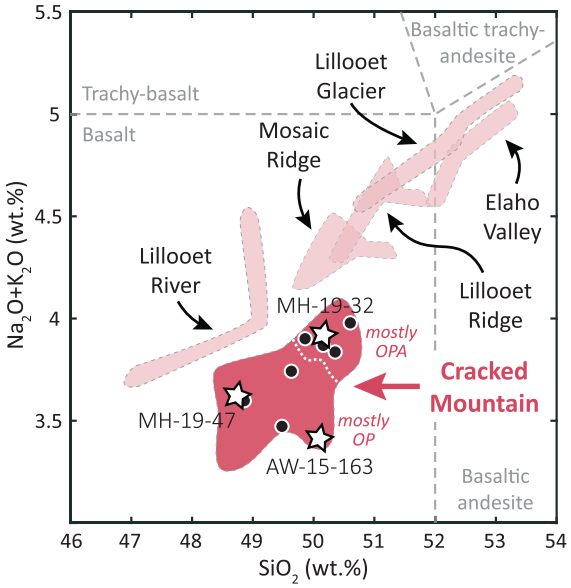

Figure 2. Total alkali silica diagram (Le Bas *et al.*, 1986) of the whole-rock compositions from the MMVC mafic centres: CM, *Lillooet Glacier*, *Lillooet Ridge*, *Lillooet River*, *Elaho Valley*, *Mosaic Ridge* (see Fig. 1b). Whole-rock analyses are from Harris *et al.* (2023), Wilson & Russell (2017), and this study. A white dotted line delineates the compositional fields where OP and OPA samples predominantly plot. The three white stars represent the CM samples used here; the black circles are the other samples from which the Fe ratios were calculated (see Table 1).

record of the Cordilleran Ice Sheet in southwestern British Columbia during the mid-Pleistocene (Harris *et al.*, 2022).

Cracked Mountain was initially mapped and described by Read (1979, 1990), who at the time grouped CM and other Pleistocene-aged, olivine-porphyritic basalts under the undivided Mosaic Assemblage. Two more thorough studies were subsequently conducted on CM, shedding light on its explosive, glaciovolcanic (Harris *et al.*, 2022), and polymagmatic (Harris & Russell, 2022) origin. The eruption was initially phreatomagmatic and then became effusive (Harris *et al.*, 2022). Furthermore, Harris & Russell (2022)'s detailed petrographic study of the CM volcanic deposits revealed that the eruption was fed by two separate crustally stored magmas, each characterised by distinct and autocrystic phenocryst assemblages: the olivine–plagioclase (OP) and the olivine–plagioclase–augite (OPA) phyric suites. Harris & Russell (2022) label samples as OP or OPA based on the prevalence (or near-absence, i.e. <3% volume) of phenocrystic augite. Accordingly, the holo- to hypocrystalline samples show predominantly glomeroporphyritic clots with plagioclase (10–15%, 0.5–3 mm) and olivine (5–10%, 0.1–1 mm) in the OP suite, with additional augite (2–5%, 0.1–1 mm) in the OPA suite; Fig. 2 in Harris & Russell (2022) provides photomicrographs illustrating representative examples of each suite. Olivine phenocrysts are subhedral and weakly zoned, while plagioclase crystals show moderate zoning, and augite crystals, when present, are subhedral. Importantly for our study, Harris & Russell (2022) showed that OP olivine phenocrysts exhibit higher forsterite ($Fo_{79–83}$) and NiO contents (0.1–0.32 wt %) than OPA phenocrysts ($Fo_{77–80}$ and NiO 0.1–0.26 wt %).

The OPA suite samples contain slightly higher SiO_2 and total alkali wt % compared to the OP suite (Fig. 2), although both share similar Rare Earth trace Element (REE) signatures, suggesting a common mantle source (Harris & Russell, 2022). Thermodynamic modelling conducted by Harris & Russell (2022) using Rhyolite-MELTS (Gualda *et al.*, 2012; Gualda & Ghiorso, 2015) indicate different pre-eruptive storage conditions, with the OP-suite magma stored at depths <7 km (<200 MPa, with a mean upper pressure of 160 MPa) at temperatures ranging from 1155 to 1240°C. In contrast, the OPA magmas crystallised at depths between 7 and 8 km (200–250 MPa, with mean conditions ranging from 190 to 240 MPa) at temperatures between 1150 and 1250°C before eruption (Harris & Russell, 2022). According to Harris & Russell (2022), both magmas were nearly dry, with H_2O contents <0.5 wt % in their respective systems. Pearce Element ratios further indicate that the chemical variations within and between the two CM magmas are controlled solely by crystal fractionation of the two phenocryst assemblages, with minor syn-eruptive mixing (Harris & Russell, 2022).

Furthermore, Harris & Russell (2022) and Harris *et al.* (2022) observed that volcanic activity at CM coincided with the waning of a global ice period and the onset of rapid global warming. They consequently suggested a correlation between the magma–crustal dynamics at CM and the paleoenvironmental processes of glacial loading and unloading characteristic of the mid-Pleistocene. In essence, the lithosphere, burdened by glacial weight, experienced magma ponding within the crust, as compressional stresses restrained volcanic eruptions (Wilson & Russell, 2020). Then, a relatively rapid phase of deglaciation ensued, resulting in crustal decompression that facilitated the eruption of magmas previously stored beneath CM.

Consequently, the detailed studies by Harris *et al.* (2022) and Harris & Russell (2022) provide a robust framework for understanding CM's eruptive history, magmatic evolution, and glaciovolcanic significance. However, questions remain regarding the fine-scale processes that shaped the magmatic plumbing system and the eruptive dynamics of CM. Through an olivine-focused lens, this study builds on their foundational work by refining constraints on the magmatic reservoirs that contributed to the CM eruption, the interactions between them and their consequences (such as crystal zoning), while also determining pre-eruptive timescales and providing new insights into the eruption's primer and trigger mechanisms.

Sampling and analytical methods

The methodologies employed in this study closely resemble those used by Aufrère *et al.* (2024), who conducted a comparable investigation on the most recent mafic centre in the MMVC, the *Lillooet Glacier* basalts (Fig. 1b).

Sample selection rationale

Three samples (*AW-15-163*, *MH-19-047*, and *MH-19-032*, see Figs 1b and 2 and Appendix A) were selected based on the following criteria: vitric nature, absence or low levels of palagonitisation, lithofacies representation, and classification into OP and OPA suites (Harris & Russell, 2022; Leiter *et al.*, 2024). CM's glaciovolcanic origin has produced diverse deposits with high glass contents including vitric breccias, lapilli tuff, pillow lavas, and dikes that cut through the massif and terminate in pillowed pods (Harris *et al.*, 2022). Vitric samples were selected as they represent material quenched upon eruption, which limits post-eruption crystal growth and diffusion, and facilitates diffusion modelling. Many available quenched samples were heavily palagonitised and thus samples showing only limited (if any) palagonitisation were

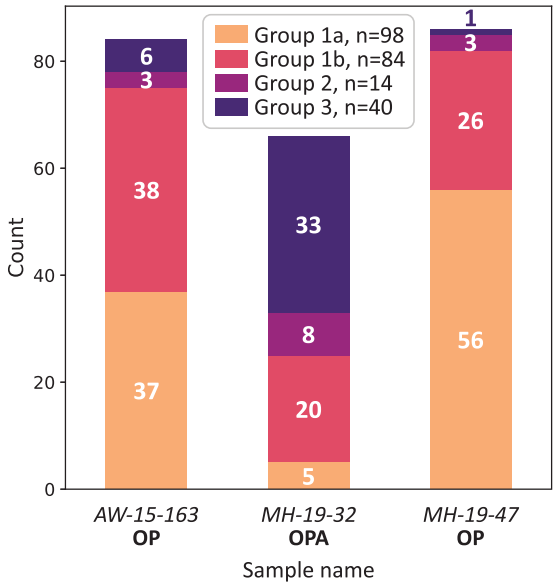

Figure 3. Distribution of the three main olivine groups (1a and 1b, 2 and 3) within the three studied samples. Note the preponderance of Group 1 in the OP samples (*AW-15-163* and *MH-19-047*) in contrast to the OPA sample (*MH-19-032*), which contains a higher proportion of Groups 2 and 3 relative to the OP samples.

chosen (Leiter *et al.*, 2024). In addition, samples were taken from different lithofacies: *MH-19-032* and *MH-19-047* are pillow lavas (with material studied from the rims), formed when lava intruded into unconsolidated and wet lapilli tuff such as *AW-15-163*, which comprises volcaniclastic sand and pillow fragments (Harris *et al.*, 2022). These samples also represent both the OP (*AW-15-163* and *MH-19-047*) and OPA (*MH-19-032*) suites (Harris & Russell, 2022; Fig. 3).

These three samples were crushed separately, with 84 olivine grains handpicked in *AW-15-163*, 66 in *MH-19-032*, and 86 in *MH-19-047*, for a total of 236 olivine crystals. They were then mounted together (each sample having its own grain-mount) and polished (see Appendix B for details). Thin sections from Harris & Russell (2022)'s *MH-19-047* and Wilson & Russell (2019)'s *AW-15-163* were used in this study, along with new polished thin sections (*MH-19-032 A, B*; *MH-19-047 A, B*) prepared by Vancouver Petrographics Ltd (Langley, BC, Canada).

Electron backscatter diffraction

Iron–Magnesium interdiffusion in olivine is anisotropic, with diffusion rates along the *c*-axis being 4–8 times faster than those along the *a*- and *b*-axes in the temperature range of 800–1200°C (Dohmen *et al.*, 2007; Dohmen & Chakraborty, 2007*a*, 2007*b*). For the purpose of accurate diffusion chronometry, it is crucial that grain orientations be determined in order to obtain reliable timescales. To achieve this, the CamScan X500FE Crystal Probe Scanning Electron Microscope (SEM) at Géosciences Montpellier (CNRS, Université de Montpellier, France) equipped with an Oxford/Nordlys Electron Backscatter Diffraction (EBSD) detector, was employed. Low-resolution montage maps of the grain-mounts (Appendix C) were obtained to record how the grain-mounts were orientated upon acquisition of the grain orientations, but also to act as a navigation and grain identification reference for subsequent analyses. To facilitate grain orientation analysis, the grain-mounts were not carbon-coated to prevent obstruction of the diffraction (Kikuchi) pattern from the olivine crystal lattices. The SEM operation was conducted in low-vacuum conditions, using an accelerating voltage range of 15–20 kV and maintaining a working distance of 20 mm. A 70° tilt, essential for optimising the diffracted signal, was ensured by using a pre-tilted column. The EBSD patterns obtained were automatically indexed using the *Channel5* software package from Oxford Instruments HKL. Most EBSD software, including *Channel5*, use the three Euler angles to describe the crystal's orientation as a series of rotations about specific axes. Upon acquiring these Euler angles, the rotational data were converted into the corresponding *a*, *b*, and *c* crystal axis orientations through the use of a custom Excel spreadsheet (*Euler-proc* Excel spreadsheet; D.J. Morgan, pers. comm., 2022). While each EBSD instrument has its own setup, the reference frame used here matched the spreadsheet's, requiring no adjustments. Subsequently, the MTEX Matlab toolbox (Bachmann & Hielscher, 2010) was employed to render 3D models of the olivine grains, orientated according to the inputted Euler angles under the Bunge convention, thereby verifying the *Euler-proc* spreadsheet outputs (see Appendix C).

Electron probe microanalysis

This study used two Electron Probe Micro-Analysers (EPMAs): a JEOL JXA-iHP200F EPMA located at The University of British Columbia (UBC) in Vancouver, British Columbia, Canada, and a CAMECA SXFive-TACTIS EPMA located at the Laboratoire Magmas et Volcans (LMV) in Clermont-Ferrand, France (the LMV system being employed until the UBC one became available). Glass analyses were conducted with the LMV EPMA, spinel with the UBC EPMA, and olivine with both instruments. The reader is referred to Aufrère *et al.* (2024) for a comparison of timescales derived from olivine profiles analysed using both EPMAs, which demonstrated that the results are comparable and well within uncertainty, with no systematic discrepancy between the two instruments. Therefore, data from both EPMAs are treated as a single, consistent dataset in this study. The analytical conditions and associated errors for each EPMA are reported in Appendix D, and the analyses from both instruments (explicitly labelled by EPMA) can be found in the complementary dataset (Aufrère & Williams-Jones, 2025).

Point analyses were carried out on the olivine cores and rims of the three grain-mounts, with the rims analysed as part of the profile end-member (see Compositional profiles section). Glass analyses were conducted to characterise the pre-eruptive melt, both randomly distributed in the *AW-15-163* thin section and in direct contact with the olivine rims in the grain-mounts, to allow for the use of these pairs for geothermometry. Additionally, spinel inclusions in olivine were analysed to evaluate potential variations in pre-eruptive conditions.

This study also aims to determine whether the embayed texture of the olivine grains is indicative of rapid growth or dissolution processes, and phosphorus (P) zoning can elucidate these aspects. For instance, rapidly grown, skeletal olivine crystals would reveal feathery, primary dendrite branches and the initial stages of infilling (Welsch *et al.*, 2014); by contrast, resorbed olivine would display irregularly cross-cut branches and, in the event of multiple dissolution occurrences, internal dissolution fronts (e.g. Fig. 2 in Mourey *et al.*, 2023). Consequently, X-ray maps of Fe, Ni, and P for selected olivine samples exhibiting embayments were collected using the UBC EPMA at an accelerating voltage of 20 kV, a probe current of 800 nA, and a dwell time per pixel of 240 ms. The beam was fully focused, which under these conditions resulted in a physical size of 250 nm (A. Von Der Handt, pers. comm., 2024). In total, five X-ray maps were obtained; the most revealing four maps (one for each olivine subgroup) are presented here. Olivine

AW-15-163 3-I was mapped with a 2-μm interval (pixel size), and *AW-15-163* gr2-J, gr5-G, and *MH-19-047* gr7-D were mapped with a 3-μm interval to reduce acquisition time.

Compositional profiles

Iron–Magnesium diffusion chronometry involves modelling forsterite ($Fo = 100 \cdot Mg/[Mg + Fe + Mn + Ca + Ni]$) profiles measured perpendicular to olivine crystal zonation. Since backscattered electron (BSE) images reveal olivine zoning through mean atomic weight variations (Reed, 2005) (with brighter pixels indicating higher Fe and darker pixels, higher Mg concentrations), high-resolution BSE images (2048 × 2048 pixels, 16 μs/pixel dwell time) were acquired with the UBC EPMA (Appendix D). These were then converted into 3-3-2 RGB images using the ImageJ software (Schneider *et al.*, 2012) to further highlight zoning (as done by Bell *et al.*, 2023; see Appendix E). Profiles were digitally mapped on each image using Adobe Illustrator for precise analysis and location record keeping (Appendix E).

Olivine EPMA profiles begin in the groundmass or 2 μm from the crystal edge, ranging from 30 to 500 μm long (average length of 150 μm), with 2- to 4-μm spot intervals (up to 12 μm for the longest profiles). However, a cost-effective alternative to EPMA profiles is BSE greyscale profiles; indeed, EPMA Fo profiles exhibit a strong negative linear correlation with BSE greyscale profiles (Martin *et al.*, 2008; Pankhurst *et al.*, 2018; Ruth *et al.*, 2018; Aufrère *et al.*, 2024). Greyscale profiles and respective traverse angles were acquired using ImageJ (Morgan *et al.*, 2004; Martin *et al.*, 2008; Hartley *et al.*, 2016; Petrone *et al.*, 2016; Rae *et al.*, 2016; Pankhurst *et al.*, 2018; Metcalfe *et al.*, 2021), with a 30-pixel-thick line tool to minimise noise (Morgan *et al.*, 2004; Pankhurst *et al.*, 2018) (see Appendix F for more details).

The BSE signal is influenced by olivine's crystallographic orientation (Joy, 1974; Lloyd *et al.*, 1987; Prior *et al.*, 1996, 1999), requiring a tailored greyscale-to-Fo calibration for each olivine grain. Thus, each EPMA Fo profile was correlated with its corresponding greyscale profile (as done in Aufrère *et al.*, 2024, see their Fig. 6a, b) to achieve the following: (1) extend limited EPMA profiles (see their Fig. 6c); (2) convert the remaining greyscale-only transects into Fo transects; (3) transform BSE images into Fo maps (similar to Cashman & Blundy, 2013's method for anorthite maps); and (4) categorise the obtained Fo maps by Fo content (using the updated *Greyscale-to-Fo* Python code, Aufrère *et al.*, 2025; see Appendix G). If a crystal had more than one EPMA Fo transect (<10%), the one with the strongest Fo–greyscale correlation ($R^2 > 0.9$) was used to convert all remaining greyscale profiles within this grain. Both extrapolated and greyscale-derived Fo transects were used for diffusion chronometry.

Acquiring multiple profiles from different crystal faces addresses anisotropic diffusion, crystal shape, and sectioning effects, thereby providing more statistically robust timescale estimates (Shea *et al.*, 2015; Aufrère *et al.*, 2024). Ultimately, we obtained 160 Fo profiles from 119 crystals of the 236 studied, including 120 EPMA-derived and 40 greyscale-derived profiles, carefully selected for optimal fits and following the guidelines set forth by Shea *et al.* (2015). Among the 119 crystals, 85 have one profile, 27 have two profiles, and 7, three profiles. The remaining 117 crystals were either analysed but deemed unsuitable for diffusion chronometry (16 crystals), or excluded from analysis due to breakage (29 crystals), unzoned, or presenting minimal Fo ranges precluding accurate diffusion profile fitting (52 crystals, predominantly belonging to Group 3, see Results), or time and financial limitations (20 crystals of lower priority as their groups were already adequately represented).

Data treatment and modelling

Pre-eruptive conditions

The diffusion rates of Fe and Mg within olivine, and consequently the calculated timescales, are highly sensitive to temperature, with pressure and oxygen fugacity having a lesser impact (Dohmen *et al.*, 2007; Dohmen & Chakraborty, 2007*a*, 2007*b*).

The application of the thermometer and fO_2 equations used in this study requires imposing constraints on the partitioning of iron between its ferrous and ferric states within the melt composition considered. Here, we use the matrix glass composition to approximate the pre-eruptive melt composition; however, glass analyses report the total iron content as FeO_T. Consequently, we estimate the partitioning of iron within the glass by imposing constraints on fresh and quenched whole-rock samples (which serve as proxies for the parental magma), assuming that the ferrous/ferric ratio remained constant from the parental magma to the pre-eruptive state (Aufrère *et al.*, 2024). Seven CM samples (*MH-19-031*, *MH-19-055*, *MH-20-001*, *MH-20-008*, *MH-20-016*, *AW-15-168*, *AW-15-178*) from Harris & Russell (2022) were analysed for both FeO and Fe_2O_3 contents (see Table 1 and Fig. 2); these do not include the three samples considered in this study (*AW-15-163*, *MH-19-047*, and *MH-19-032*). Furthermore, although *MH-19-047* and *MH-19-032* whole-rock compositions are published in Harris & Russell (2022) (and reported in Table 1), *AW-15-163* had not yet been analysed. The three samples considered here were thus processed by ALS Global in North Vancouver (BC, Canada) for FeO content measured volumetrically by titration, and whole-rock composition of *AW-15-163* (analyses are reported in Table 1).

For modelling purposes, we assume an isothermal system. Temperature estimates were obtained using geothermometers that are both pressure- and water-dependent (Beattie, 1993; equation 4 from Putirka *et al.*, 2007). Therefore, both pressure (P) and water constraints are required, which we adopt from the pre-eruptive P-H_2O storage conditions of Harris & Russell (2022): mean upper pressures of 160 MPa for the OP magma, and 240 MPa for the OPA magma, with H_2O contents <0.5 wt % (see Appendix H for how Harris & Russell, 2022 constrained these conditions). While diffusion likely occurred at slightly lower pressures, pressure variations have a negligible effect on timescales, as discussed in Appendix H. To account for water dependence in thermometry, we applied the anhydrous geothermometer of Beattie (1993) at 0 wt % H_2O and equation 4 from Putirka *et al.* (2007) at 0.5 wt % H_2O, as these provide the best estimates for anhydrous and hydrous conditions, respectively (Putirka, 2008; Appendix I). Calculations were performed using the open-source Python3 package *Thermobar* v1.0.67 (Wieser *et al.*, 2022), considering only olivine–liquid pairs with K_D values in the 0.27–0.33 range (Roeder & Emslie, 1970) (Appendix I Table A.7).

The oxygen fugacity was constrained based on iron partitioning, temperature, and groundmass glass composition, rearranging equation 4 from Borisov *et al.* (2018). We then expressed the fO_2 values in terms of ΔNNO and ΔFMQ (Frost, 1991; Huebner & Sato, 1970; Iacovino, 2022 and references therein; Appendix I Table A.8; Table 2). These calculations were performed using the same fixed pressures of 160 MPa for OP crystals (Group 1; see Results) and 240 MPa for OPA crystals (Group 2; see Results), with temperatures constrained as previously described.

Diffusion modelling

The Excel-based AUTODIFF model was used to calculate timescales from Fe–Mg interdiffusion in olivine (see Couperthwaite *et al.*, 2020 for a comprehensive description

Table 1: Whole-rock major element compositions (wt %) of the CM volcanic rocks used to calculate the Fe ratios

Sample ID	AW-15-163	MH-19-047	MH-19-032	MH-19-031	MH-19-055	MH-20-001	MH-20-008	MH-20-016	AW-15-168	AW-15-178
UTM East	460 805	460 450	460 964	460 964	461 014	460 535	460 462	460 551	460 545	460 807
UTM North	5 599 591	5 599 594	5 599 860	5 599 860	5 599 824	5 599 657	5 599 597	5 599 924	5 599 555	5 599 494
SiO_2	48.3	49.24	50.04	50.16	49.97	49.76	49.66	48.62	50.22	48.91
TiO_2	1.5	1.59	1.54	1.33	1.46	1.51	1.49	1.41	1.50	1.4
Al_2O_3	14.5	15.44	15.47	15.23	15.34	15.33	15.4	15.54	15.42	15.02
Fe_2O_3 [a]	3.68	3.38	2.11	2.01	2.25	2.13	2.82	2.81	2.16	2.31
FeO [b]	8.61	8.81	8.8	9.01	9	9.41	9.03	9.14	8.64	8.08
MnO	0.17	0.16	0.15	0.15	0.16	0.16	0.16	0.15	0.15	0.15
MgO	8.71	8.39	7.69	9.11	8.72	8.78	8.77	9.23	8.05	9.72
CaO	7.77	9.1	8.85	8.56	8.62	8.59	8.74	8.77	8.94	8.56
Na_2O	2.85	3.3	3.13	3.18	3.05	3.22	3.14	3.27	3.19	3.05
K_2O	0.44	0.36	0.78	0.64	0.8	0.67	0.6	0.31	0.75	0.38
P_2O_5	0.26	0.28	0.25	0.24	0.24	0.25	0.24	0.25	0.23	0.23
Totals	100.32	101.03	99.79	100.74	100.76	101.03	101.17	100.61	99.04	98.72
LOI	2.45	−0.37	−0.19	−0.31	−0.37	−0.49	−0.37	−0.52	0.36	0.77
FeO(T)	11.92	11.85	10.70	12.02	12.25	12.59	12.86	12.97	10.59	11.29
$Fe^{3+}/\Sigma Fe$ [c]	0.28	0.26	0.18	0.17	0.18	0.17	0.22	0.22	0.18	0.20
Fe^{3+}/Fe^{2+} [c]	0.38	0.35	0.22	0.20	0.22	0.20	0.28	0.28	0.22	0.26

Whole-rock analyses conducted by Acme Labs Ltd., Vancouver, BC (all but the *AW-15-163* sample; Harris & Russell, 2022), and by ALS Canada Ltd., North Vancouver, BC (*AW-15-163*; this study). Coordinate system: UTM Projection 10 N (metres); WGS84 Datum.
[a]Fe_2O_3 calculated for samples with known FeO, where $Fe_2O_3 = (FeO_T\text{-}FeO)/0.8998$.
[b]FeO determined separately through ferric titration, measured by ALS Canada Ltd., North Vancouver, BC for all samples. *AW-15-163*, *MH-19-047*, and *MH-19-032* FeO contents were obtained in this study; the others are from Harris & Russell (2022).
[c]$Fe^{3+}/\Sigma Fe$ and Fe^{3+}/Fe^{2+} ratios calculated from molar Fe^{3+} and Fe^{2+} abundances derived from major-element compositions.

Table 2: Olivine–liquid equilibrium temperature and oxygen fugacity conditions constrained for each olivine–liquid group

H_2O	0 wt %	0.5 wt %
Group 3 core - Average thin-section glass	1144 ± 44 °C	1137 ± 29 °C
	ΔNNO = 0.6 ± 1.1	ΔNNO = 0.6 ± 1.1
Group 1a rim - Touching glass	1139 ± 44°C	1132 ± 29°C
	ΔNNO = 0.6 ± 1.1	ΔNNO = 0.6 ± 1.1
Group 1b rim - Touching glass	1139 ± 45°C	1133 ± 30°C
	ΔNNO = 0.6 ± 1.1	ΔNNO = 0.6 ± 1.1
Group 2 rim - Touching glass	1142 ± 44°C	1137 ± 29°C
	ΔNNO = 0.5 ± 1.1	ΔNNO = 0.6 ± 1.1
Group 3 rim - Touching glass	1137 ± 44°C	1131 ± 29°C
	ΔNNO = 0.6 ± 1.1	ΔNNO = 0.6 ± 1.1

Pressure is set at 160 MPa for Group 1 and 3, and 240 MPa for Group 2. Temperatures calculated using Beattie (1993) when $H_2O = 0$ wt %, and equation 4 of Putirka *et al.* (2007) when $H_2O = 0.5$ wt %. Oxygen fugacity calculations use equation 4 from Borisov *et al.* (2018). Conditions obtained for the olivine rims/touching glass pairs are those used for the diffusion chronometry calculations.

of AUTODIFF and its demo version). There are currently two versions of AUTODIFF: one is designed to portray a homogeneous crystal experiencing diffusion and re-equilibration from the edge (under the assumption of no growth and diffusion only), and the other considers a step-like function with a homogeneous core and a compositionally distinct rim (assuming that rim formation occurred rapidly enough to isolate the core-rim interface from the melt before significant diffusion occurred). Although the reality likely lies somewhere between these extremes, typically, one end-member solution prevails over the other, indicating a predominant process. This study employs both configurations, opting for the one that most accurately fits the zoning pattern observed in individual crystals. Most crystals (76 out of 119) are best modelled as homogeneous crystals subject to diffusion and re-equilibration from the edge. In contrast, the remaining 43 crystals exhibit a pronounced curvature in the diffusion profile that extends away from the core, along with the presence of an inflection point in the profile gradient near the rim. This observation suggests that these crystals were likely influenced by crystal growth and/or variable boundary conditions (such as changes in cooling rates) concurrent with diffusion, as noted in Couperthwaite *et al.* (2021). Consequently, these cases align more closely with the step-like function configuration.

The majority of the diffusion profiles (75%) exhibit a very close alignment with one of the two AUTODIFF model configurations. The remaining profiles (25%), although adequately fitted, would benefit from incorporating variations in boundary conditions in addition to growth rates, as these are known to influence the shape of diffusion profiles (e.g. quadrupling the cooling rate results in a halving of the diffusion width, and initial growth widens the profiles; Couperthwaite *et al.*, 2021). While there have been recent advancements in this modelling (see Couperthwaite *et al.*, 2021; Kahl *et al.*, 2023), this more sophisticated approach requires inputs (e.g. parental melt composition, growth, and cooling rates) that are not sufficiently well constrained for application here due to the limited geochemical investigations undertaken within the MMVC.

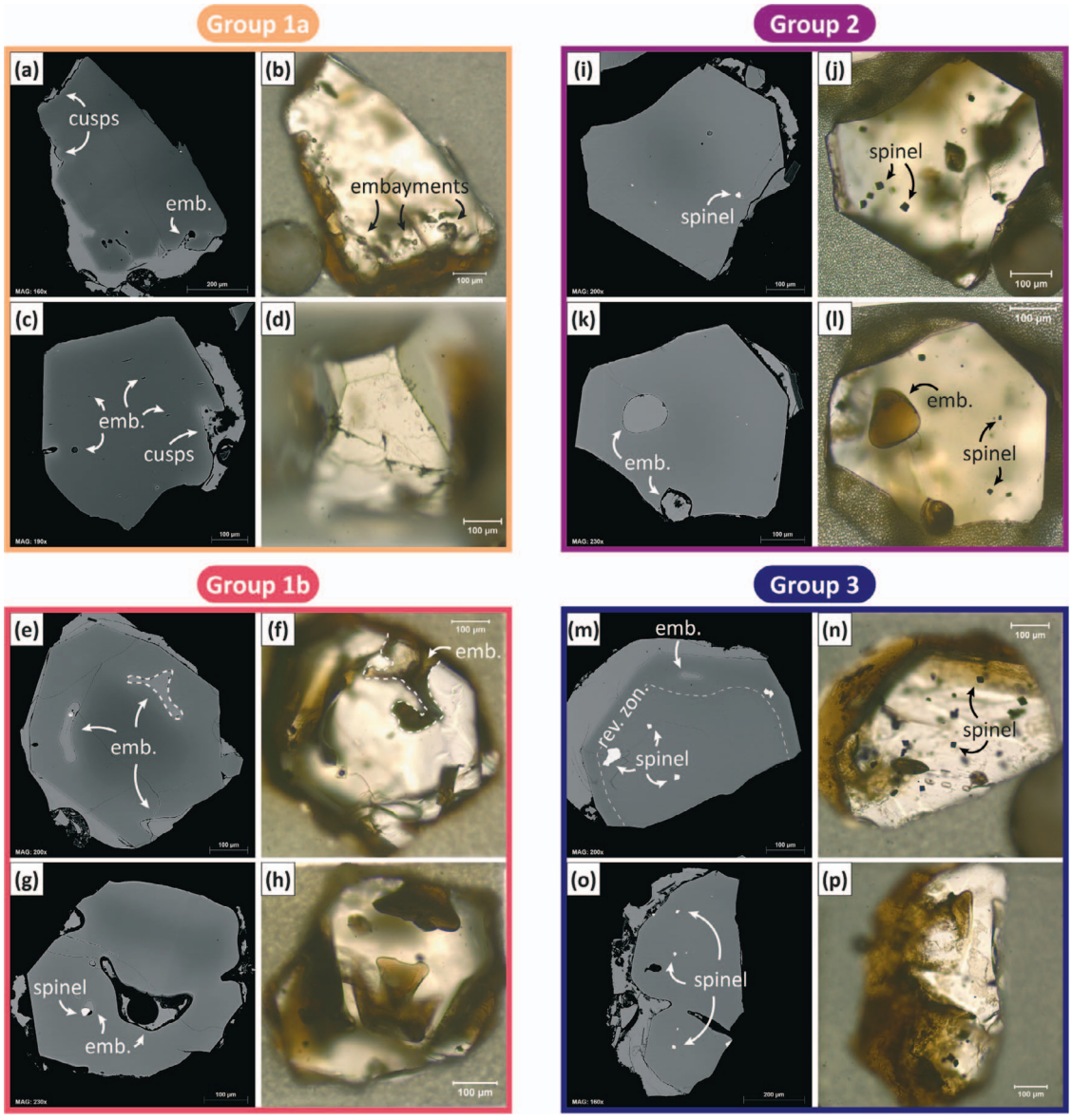

Figure 4. Examples of BSE images of olivine sections alongside images of the back of the same mounted olivine grains, captured using a petrographic microscope under transmitted light. Two representative grains from each of the subgroups (1a, 1b, 2, and 3) are shown. Subgroup 1a (a– d) displays olivine crystals characterised by cuspate margins (cusps) and embayments (emb.). It is noteworthy that despite (c) presenting embayments, it retains a close-to-euhedral crystal form (d). Subgroup 1b (e–h) also shows embayments, though their connectivity with the crystal exterior is not always clear (e, dashed lines) but becomes evident when observed through a petrographic microscope (f). Skeletal olivine crystals are more readily discernible via petrographic microscopy (f, h) compared to BSE images (e, g, respectively), despite the presence of embayments. This occurs because petrographic microscopes allow for focusing at various depths within the grains, whereas BSE images are limited to the polished section. Lastly, Group 2 (i–l) and Group 3 (m–p) are notable for their numerous spinel inclusions (i–p), with Group 3 exhibiting skeletal characteristics (p), and rarely, inner reverse zoning (m, rev. zon.).

The consistency of timescales within a single grain is shown in Aufrère *et al.* (2024), but zoning stretch due to shallow sectioning often results in an apparent profile distance longer than the true length (Costa & Morgan, 2010; Couperthwaite *et al.*, 2021). Thus, we used the narrowest diffusion profile for each crystal in AUTODIFF to mitigate sectioning effects. The rim-to-core profile inputs for AUTODIFF were derived from either EPMA-based and greyscale-extended profiles, or greyscale-derived-only profiles (converted to Fo values). AUTODIFF applies the corrected Fe–Mg diffusion coefficients from Dohmen & Chakraborty (2007*b*), which account for composition, pressure, temperature (T), fO_2, and anisotropy. The Fo core and rim compositions are grain-dependent, with the Fo_{core} end-member corresponding to the beginning of the plateau, and the Fo_{rim} marking the end of the steep decline in Fo values (as crystals are normally zoned). Pressure, T, and fO_2 were set to be constant within each olivine group, using the pressure estimates from Harris & Russell (2022) (i.e. $P = 160$ MPa for OP crystals, and $P = 240$ MPa for OPA crystals) and the temperatures and oxygen fugacity constrained in this study (see Table 2). Lastly, anisotropy was handled through crystal orientations obtained via EBSD.

Results

Olivine

Cracked Mountain olivine phenocrysts are found as single crystals (up to 3 mm in length) or as part of olivine-only, OP, or OPA

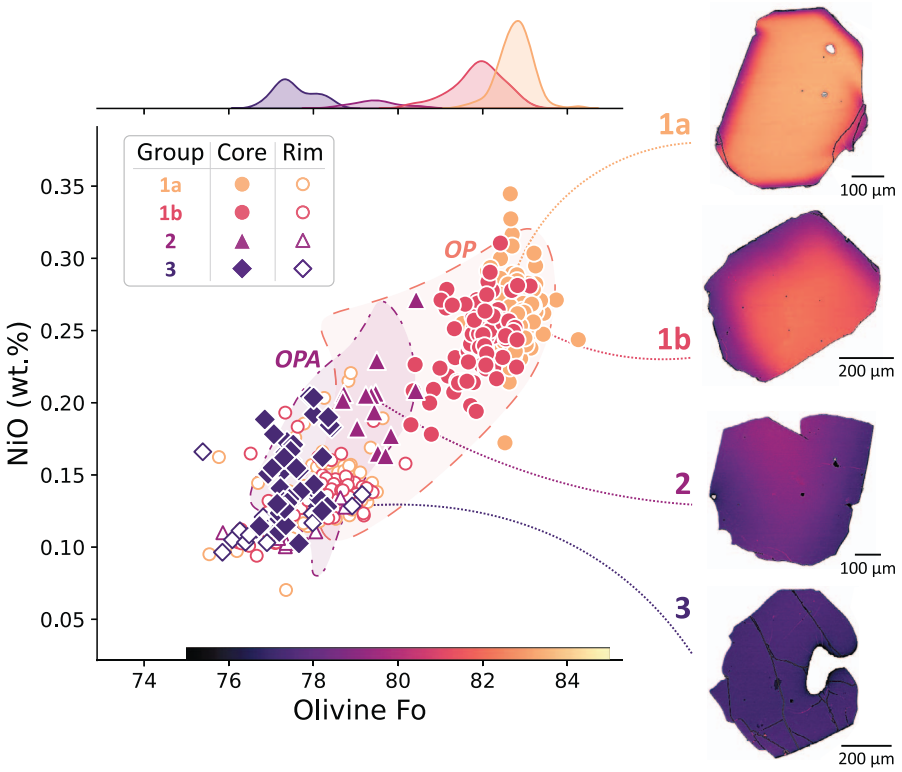

Figure 5. Chemical multimodality of the three main olivine populations (Group 1a/b, 2, and 3) observed within the CM samples. These are plotted against their Fo and NiO content, with Kernel Density Estimation (KDE) plots for the core compositions shown on the opposite axis. Group 1a and 1b are considered as part of the same population due to their chemical and textural similarities. Data from Harris & Russell (2022) (OP and OPA fields) and this study.

glomerocrysts. In the *AW-15-163* tephra sample, glomerocrysts are uncommon, with single and broken olivine crystals being more prevalent. In contrast, the *MH-19-047* and *MH-19-032* pillow lava samples contain large (3–6 mm) OP glomerocrysts, and olivine-only glomerocrysts are common. In only one of the three *MH-19-047* thin sections, two large (6 mm) OPA glomerocrysts were observed. Furthermore, very rare occurrences of single, augite crystals were found in two of three *MH-19-047* thin sections and in one of two *MH-19-032* thin sections. In all cases, augite crystals appear subhedral or rounded, with their core sometimes slightly sieve-textured. Interestingly, spinel oxide inclusions are present within the OPA glomerocrysts: many are included in olivine and augite crystals, and fewer in the plagioclase crystals. However, these spinel inclusions are rare in the OP glomerocrysts.

Regardless of what glomerocrysts they are part of, the olivine crystals range from euhedral (a very small number of grains; e.g. Fig. 4d and m) to subhedral in shape (e.g. Fig. 4g and o). A significant portion of the crystals observed in thin sections and grain-mounts are embayed (183 of the 236 studied), with many showing typical skeletal features such as straight edges, angular corners, and embayments that create arrow-shaped (Fig. 4h and p) or more intricate cross-sections.

Three main olivine groups (later referred to as Group 1a/b, 2, and 3; Fig. 5) were discerned using the *BSE-to-Fo-image_clustering* Python code (Aufrère *et al.*, 2025; Appendix G), based on the overall Fo distribution within each crystal section. These groups are distributed differently across the three samples: Group 1a ($n = 98$) and 1b ($n = 84$) are largely present in *AW-15-163* and *MH-19-047*; Group 2 ($n = 14$) is rare overall but proportionally more common in *MH-19-032*; and Group 3 ($n = 40$) dominates *MH-19-032*, with only a few crystals present in *AW-15-163* and *MH-19-047* (Fig. 3).

Compositional variations

Group 1a and 1b exhibit overlapping core and rim compositions and are differentiated solely on the nature of their zoning (Figs 5 and 6a and b). Specifically, Group 1a comprises normally zoned (both in terms of Fo and NiO, see Fig. 6e and g) olivine crystals with short diffusion widths (on average 120 µm) and a core composition centered on Fo_{83} and 0.2–0.3 wt % NiO (Figs 5 and 6a). In contrast, while Group 1b olivine crystals are also normally zoned (again, both in terms of Fo and NiO, see Fig. 6f and h), they show greater diffusion widths (~170 µm) and a slightly more evolved core, centered on Fo_{82}, with similar NiO contents (0.2–0.3 wt %) (Figs 5 and 6b). Both Groups 1a and 1b cores plot within the OP field defined by Harris & Russell (2022), with rim compositions mostly within the $Fo_{76–79}$ and 0.10–0.15 wt % NiO range (Fig. 5). While 75% of Group 1a show a better fit with the AUTODIFF diffusion-only model (Fig. 6g), 54% of Group 1b show a better fit with the step-like function model assuming rapid growth and then diffusion (Fig. 6h). In such instances, a plateau in Fo and NiO concentrations is established at the olivine rims (Fig. 6f and h). Additionally, a minor subset of crystals (3% of Group 1a, and 9% of Group 1b crystals with an available diffusion profile) display a subtle Fo reverse zoning at their outer rim (indicated by a 0.3–1.3 Fo increase towards the rim; e.g. Fig. 6d and h). Interestingly, NiO rarely correlates with the reverse zoning trend but either is constant or continues to decrease normally (e.g. Fig. 6f).

Group 2 olivine cores have lower Fo and NiO compositions than those of Group 1 ($Fo_{79–81}$ and 0.15–0.25 wt % NiO), plotting within the OPA field defined by Harris & Russell (2022) (Fig. 5). These crystals exhibit slight normal zoning in both Fo and NiO, with diffusion widths of ~150 µm (e.g. Figs 7a, e, g and 8a, b), and rims

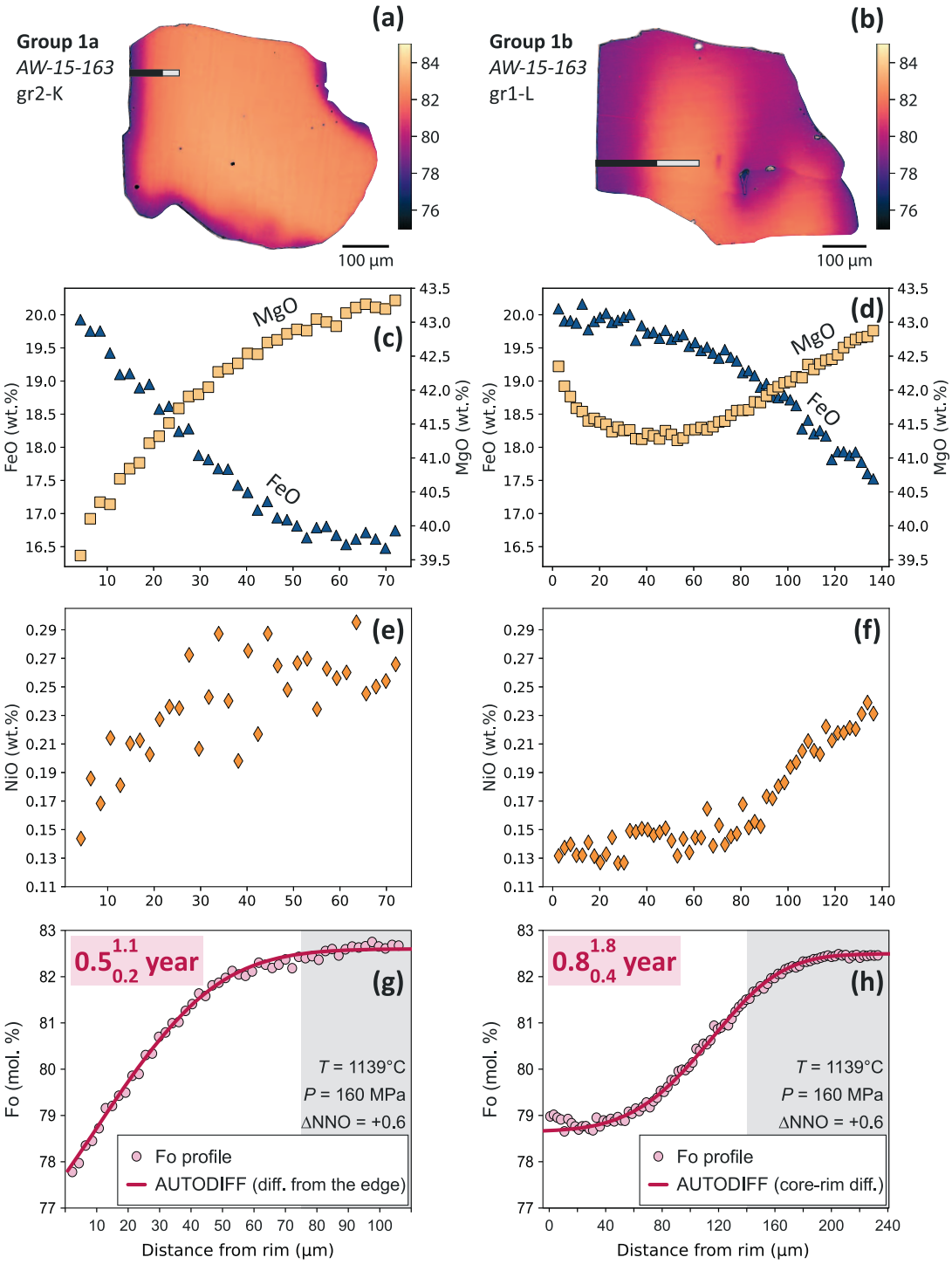

Figure 6. Examples of compositional profiles for Group 1a and 1b olivine crystals. Panels (a, b) show Fo maps derived from BSE images (processed via Python code; Aufrère *et al.*, 2025), with (b) demonstrating more extensive diffusion widths than (a). Bars perpendicular to the crystal rim delineate the locations of the compositional profiles presented in panels (c) through (h). The black segment of each bar signifies measurements obtained via EPMA while the grey section is extrapolated based on the BSE image, its greyscale, and the greyscale-to-Fo Python code. Consequently, only the Fo values (and not MgO, FeO, or NiO) are available for this portion of the profile, and reach a plateau. Panels (c, d) show the variations in FeO (triangles) and MgO (squares) compositions along these profiles: both crystals exhibit a main, normal zoning characterised by a decrease in MgO and an increase in FeO towards the crystal rims. However, in (d) there is an additional increase in MgO coupled with a less pronounced FeO increase towards the outermost rim. Panels (e, f) present the NiO (diamonds) compositional changes along the same profiles: in (e), NiO follows the MgO trend, decreasing towards the rim; whereas in (f), a shift in the NiO gradient is observed, continuing its decrease but with a significantly reduced steepness. Panels (g, h) show the Fo (circles) content along these profiles, demonstrating main normal zoning fitted with two AUTODIFF models: the one considering diffusion (diff.) from the edge in (g), and the core–rim, step function diffusion model in (h). The grey shaded area in the core-direction segment of the Fo profiles represents the extrapolated segment based on greyscale analysis, using the greyscale-to-Fo Python code. Minimum timescales obtained through AUTODIFF at 1139°C, 160 MPa, and NNO + 0.6 are shown in the upper left corner of (g, h), with timescales in subscript representing the lower bound of the uncertainties, and superscript being the upper bound. Note a very slight reverse zoning towards the rim edge in panel (h). The point symbols shown in (c–h) are larger than their related uncertainties.

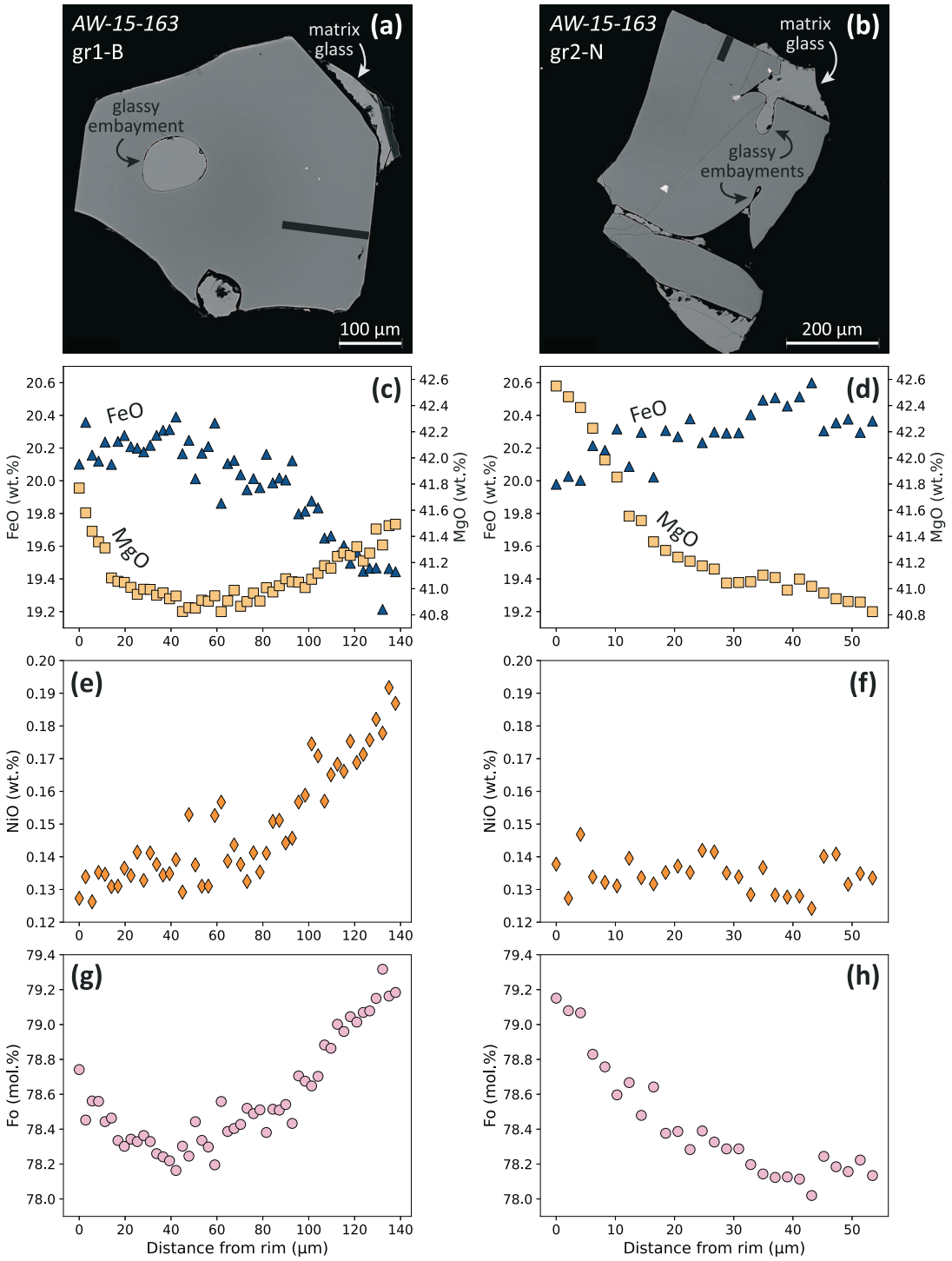

Figure 7. Examples of Group 2 (left column) and 3 (right column) olivine crystals, showing minor Fo reverse zoning at their outermost rims. Panels (a, b) present their BSE images; (a) displays a minor greyscale variation between the darker core and the lighter rim, whereas (b) shows a consistent grey tone. Black rectangles perpendicular to the crystal rim delineate the locations of the EPMA compositional profiles presented in panels (c) through (h). Panels (c, d) depict the evolution of FeO and MgO compositions along these profiles, showing a decrease in FeO content and an MgO increase towards the rim. Panels (e, f) show the NiO evolution along the same profiles: in panel (e), a change in the NiO slope is observed (continuing to decrease, albeit less sharply), while in (f), the composition of NiO remains constant. Finally, panels (g) and (h) show the Fo content along these profiles, both indicating a distinct increase in Fo towards the outermost rim (i.e. a reverse zoning).

that overlap the Fo and NiO range of Group 1 (Fig. 5). For most profiles (75%), this zoning is best reproduced by the diffusion-from-the-edge AUTODIFF model. Additionally, 75% of the Group 2 crystals for which an Fo profile was obtained exhibit faint outer reverse zoning, indicated by a ~0.5-Fo increase towards the rim (Figs 7g and 8a). Similarly to the trends observed in Group 1, the Fo and NiO patterns in the reverse Fo zoning of Group 2 rarely correlate (Fig. 7e and g).

Group 3 olivine crystals are characterised by the lowest Fo core contents (centred on $Fo_{77–78}$; Fig. 5), which are in equilibrium with the glassy groundmass (see Fig. A.22 in Appendix). They generally lack inner zoning (Figs 5, 7b, and 8a, b), with the exception of

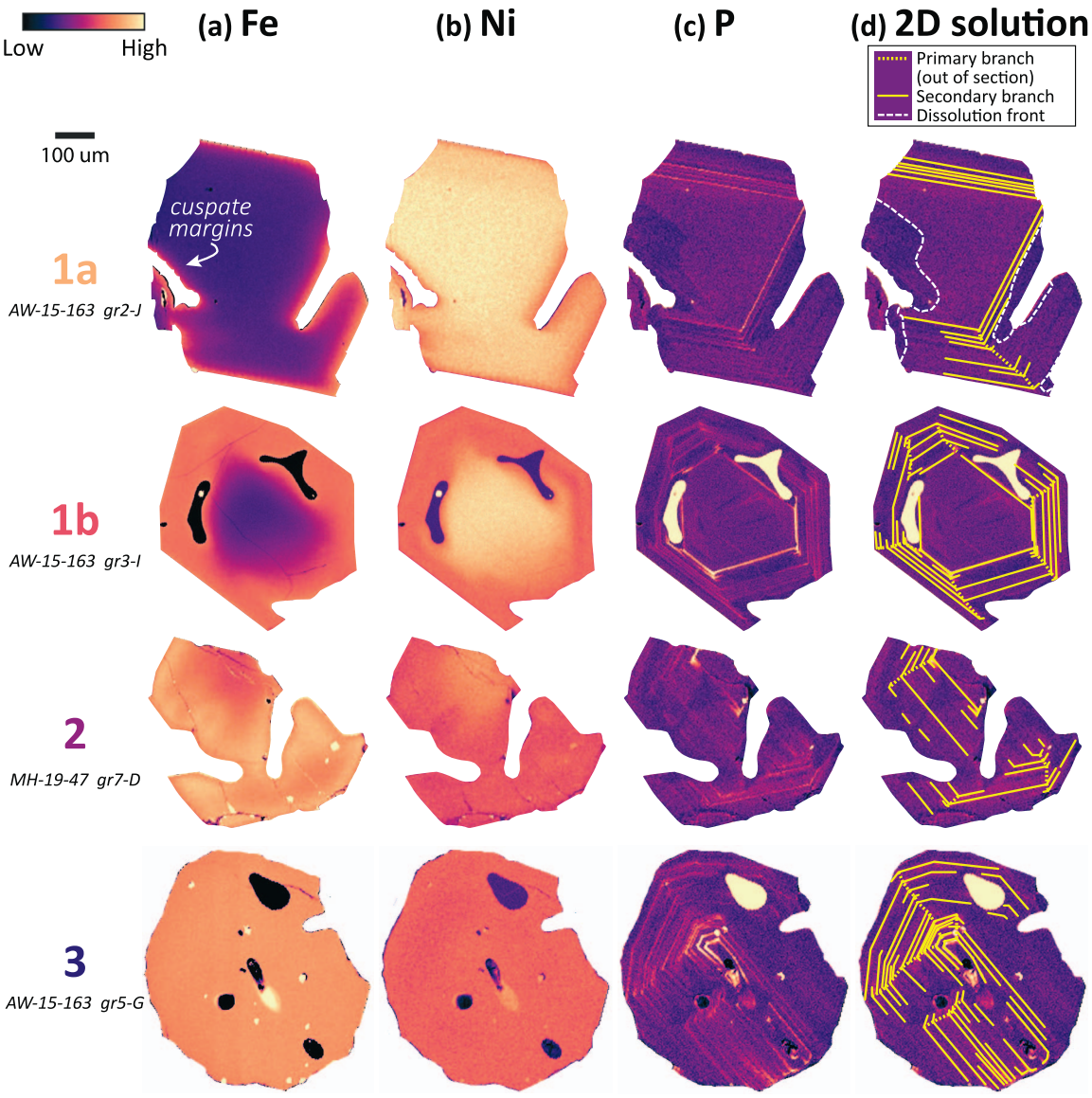

Figure 8. Compositional maps of a representative crystal from each of the four identified olivine groups (1a, 1b, 2, and 3), illustrating the distribution of (a) iron (Fe), (b) nickel (Ni), and (c) phosphorus (P). Column (d) presents an interpretation of the P-maps (shown in c), highlighting the primary (dotted yellow lines) and secondary (solid yellow lines) branches, which are the initial structures formed during olivine growth. Additionally, dissolution fronts (dashed white lines) are identified, indicating zones where branches have undergone resorption and been replaced by low-P olivine. The cuspate margins observed in the Group 1a olivine crystal are also indicated.

one grain that displays inner reverse zoning ($Fo_{78.3}$–$Fo_{78.9}$ across 30 μm) prior to normal zoning on its last outer 30 μm (Fig. 4m). As a result, diffusion chronometry was not applicable to this group. Despite the absence of resolvable inner zoning, ~35% of the Group 3 crystals for which Fo profiles were acquired display subtle outer rim reverse zoning, expressed as a 0.6–1.2 Fo increase towards the rim (Fig. 7h). In line with Groups 1 and 2, Fo and NiO variations within these reversely zoned rims are largely decoupled (e.g. Fig. 7f and h). For all groups, since this outer rim reverse zoning is subtle (mostly <1 mol % Fo) and generally spans <10 analyses, it prevents reliable fitting with diffusion models. No timescales were thus retrieved for this late-stage event.

Textural variations

A significant proportion of Group 1 crystals exhibit embayments (Fig. 4a–h), specifically 84% in the Group 1a population and 79% in the 1b population. In addition, some Group 1 grains display cuspate margins in their sections (18% of Group 1a, and 8% of Group 1b; e.g. Fig. 4a and c). One of the Group 1a crystals exhibiting cuspate margins is shown in Fig. 8a; additionally, its P-map reveals zones of low phosphorus concentration cutting through the crystal's secondary branches (i.e. its skeleton; Fig. 8d). In contrast, the P-map of a Group 1b crystal shows very clear primary and secondary branches, with embayments located within growth zones (Fig. 8d). In its section, the embayments appear as elongated melt inclusions (Fig. 8); however, upon observation via a petrographic microscope with the focus adjusted for depth, the connections to the exterior of the crystal become evident (Fig. 4e and f). Additionally, 19% (22% in the 1a population, 15% in the 1b) of the Group 1 crystals corners are rounded, and 16% (14% crystals in the Group 1a, 18% in the Group 1b) are angular, although most grains are too broken to accurately assess their overall shape. Lastly, by adjusting the petrographic microscope focus to gauge how far grains extended below the surface, we found that 28% of

Group 1a and 33% of Group 1b crystals are exposed at shallow levels. In these cases, the section likely does not pass through the crystal core, which may influence textural and compositional interpretations.

No cuspate margins are observed on the Group 2 crystals; however, the majority (71%) of them exhibit embayed features (e.g. Fig. 4k and l), some of which possibly associated to fast growth (Fig. 8d). Regarding the crystal's corners, 14% of the Group 2 crystals are rounded (e.g. Fig. 4k and l) and 21% displaying angular corners (e.g. Fig. 4i and j), while the rest of the grains are too broken to determine their original morphology. For 21% of the crystals, their section can be considered superficial.

A similar distribution of textural features is observed in Group 3 crystals. Cuspate margins are absent, and embayments are present in 63% of the grains (e.g. Fig. 4m) and commonly associated with skeletal textures (Figs 4p and 8d). With respect to crystal corners, 25% of the grains display rounded corners and 18% preserve angular corners (e.g. Fig. 4m), although most crystals are too fragmented to reliably assess their original morphology. In addition, 35% of the Group 3 crystals are superficially sectioned.

Spinel and sulphide inclusions

Inclusions of Fe–Ni(-Cu) sulphide were identified under reflected light by their higher reflectivity, metallic or brown–purple lustre, lower relief, and globular or irregular shapes (see Appendix J), while spinel showed lower reflectivity, non-metallic lustre, higher relief, and blocky euhedral shapes. On average, the spinel group oxides inclusions described in the following paragraphs are $Mg^{\#}{}_{42}$, $Cr^{\#}{}_{37}$, and $Fe^{3+\#}{}_{28}$ (Fig. 9; with $Mg^{\#} = 100 \cdot Mg/[Mg + Fe^{2+}]$, $Cr^{\#} = 100 \cdot Cr/[Cr + Al + Fe^{3+}]$, and $Fe^{3+\#} = 100 \cdot Fe^{3+}/[Cr + Al + Fe^{3+}]$). Their substantial concentrations in Cr_2O_3, FeO, and Al_2O_3 point to compositions indicative of chromite or aluminochromite varieties.

Group 1 olivine crystals show very few spinel inclusions (if any), with only a single inclusion per section identified in 16% of the Group 1a sections (17 μm in size on average), and in 32% of Group 1b (~13 μm). Interestingly, these spinel inclusions only occur in the olivine rims, embayments (Fig. 4g), or on crystal edges (Fig. 8, Group 1a). Spinel oxides located within the Group 1 olivine rims exhibit compositions of $Cr^{\#}{}_{34.4–37.6}$, $Mg^{\#}{}_{38.6–50.3}$, $Fe^{3+\#}{}_{20.9–30.1}$, and Ti contents ranging between 0.03 and 0.10 p.f.u. (per formula unit) (Fig. 9). In comparison, those located on crystal edges or within embayments exhibit compositions up to $Cr^{\#}{}_{41.4}$, $Fe^{3+\#}{}_{32.7}$, 0.12 p.f.u. Ti, at $Mg^{\#}$ down to $Mg^{\#}{}_{37.5}$ (Fig. 9). Additionally, some 10- to 60-μm sulphide inclusions were identified in 12% of Group 1a crystals and 12% of Group 1b crystals (Fig. A.28 in Appendix J).

In contrast, no sulphide inclusions are observed within Group 2 and 3 olivine crystals. Rather, these are characterised by a high occurrence of ~17-μm (Group 2) and ~2-μm (Group 3) spinel inclusions in their cores, rims, embayments, and on the edges (Fig. 4i-p), with 68% of the grains displaying ~10 inclusions in their section. Regardless of the spinel inclusion locations, Group 2 and 3 olivine crystals show overlapping compositions of $Cr^{\#}{}_{32.5–41.8}$, $Mg^{\#}{}_{36.9–48.4}$, $Fe^{3+\#}{}_{23.8–34}$, with Ti-contents ranging between 0.03 and 0.12 p.f.u. (Fig. 9).

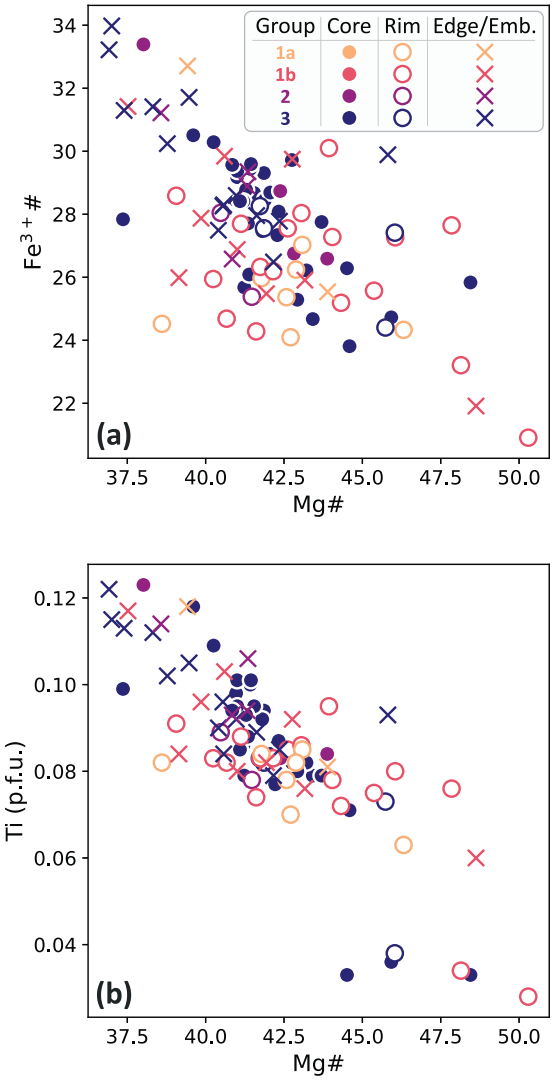

Figure 9. Compositions of spinel inclusions within olivine, illustrated by plotting (a) $Fe^{3+\#}$ and (b) Ti content (p.f.u) against their $Mg^{\#}$ content. The spinel inclusion labels are based on their locations within the olivine crystals: either in the core (solid circles; note that Group 1 lacks spinel inclusions in their core), the rim (open circles), embayments, or situated directly on the crystal edge. The latter two categories are collectively represented by the cross symbol.

Diffusion chronometry

Pre-eruptive conditions

The $Fe^{3+}/\sum Fe$ ratios for the three samples in this study are as follows: 0.28 for *AW-15-163*, 0.26 for *MH-19-047*, and 0.18 for *MH-19-032* (see Table 1). Compared to the seven samples analysed by Harris & Russell (2022) (Table 1), which averaged 0.19 ± 0.02, *AW-15-163* and *MH-19-047* appear more oxidised. These two samples are the glassiest in our study; their direct contact with water upon eruption might explain their higher ratios. Therefore, for subsequent thermometry calculations, we used the *MH-19-032* ratio and those from Harris & Russell (2022), for an average ($n = 8$) $Fe^{3+}/\sum Fe = 0.19 \pm 0.02$. This ratio corresponds with that documented for the neighboring *Lillooet Glacier* (Fig. 1b) eruption (obtained via the same method; Aufrère *et al.*, 2024), and is lower than the 0.26–0.28 range reported for another mafic MMVC center, *Mosaic Ridge* (Fig. 1b) (inferred from olivine-hosted melt inclusions; Venugopal *et al.*, 2020). Consequently, both the *Lillooet Glacier* and CM eruptions occupy the lower spectrum of the 0.18–0.32 $Fe^{3+}/\sum Fe$ range characteristic of subduction zones (Kelley & Cottrell, 2009). This averaged ratio from the select CM samples was then used in *Thermobar* (version 1.0.67, Wieser *et al.*, 2022) to evaluate the olivine–liquid equilibrium among the three subgroups. The olivine–liquid pairs were then filtered (K_D within the range of 0.27–0.33; Roeder & Emslie, 1970) to ensure the

accuracy of the temperature constraints (Table A.7 and Fig. A.22 in Appendix I).

As previously noted, the thermometry calculations used the thermometer from Beattie (1993) under anhydrous conditions, and equation 4 from Putirka *et al.* (2007) for $H_2O = 0.5$ wt %. The applied pressures (discussed in Appendix H) are 160 MPa for Group 1 and 3, and 240 MPa for Group 2, based on the storage pressure constraints of the OP and OPA magmas established by Harris & Russell (2022). The fO_2 conditions were constrained using equation 4 from Borisov *et al.* (2018). The resulting temperature and oxygen fugacity conditions are summarised in Table 2 (see Appendix I for more details); for diffusion chronometry, we used the conditions obtained for the olivine rims/touching glass pairs. The oxygen fugacity constrained (between NNO + 0.5 and NNO + 0.6, ± 1.1) aligns with the NNO + 0.5 pre-eruptive conditions similarly obtained for the neighbouring volcanic center, *Lillooet Glacier* (Fig. 1b; Aufrère *et al.*, 2024). Likewise, the oxygen fugacity conditions observed in this study closely resemble the NNO + 0.74 conditions derived from olivine-hosted melt inclusions at *Mosaic Ridge* (Fig. 1b; Venugopal *et al.*, 2020). Furthermore, the temperatures documented in Table 2 fall on the lower end of the range estimated by Harris & Russell (2022) at CM (1155–1240°C for the OP suite, and 1150–1250°C for the OPA suite), on the higher end of the *Mosaic Ridge* range (1057–1142°C; Venugopal *et al.*, 2020), and exceed the pre-eruptive temperature estimated at *Lillooet Glacier* (Fig. 1b), ~1100 ± 30°C (Aufrère *et al.*, 2024).

Timescales

The rim/glass contact temperatures and oxygen fugacity conditions were input into AUTODIFF, along with the pressure constraints from Harris & Russell (2022). Resulting timescales are presented as minimum and maximum: the minimum timescale corresponds to the temperature calculated when $H_2O = 0$ wt %, and the maximum to the temperature when $H_2O = 0.5$ wt % (see Fig. A.21 and Excel sheets I1, 2, and 3 in Appendix I, for input parameters, model fits, and calculated timescales).

Of the 119 crystals with analysed diffusion profiles, 61 belong to Group 1a, 54 in Group 1b, and only 4 in Group 2 (there are only 14 crystals in Group 2, and several exhibit minimal Fo ranges that prevent accurate diffusion profile fitting). Diffusion modelling with AUTODIFF on Group 1 reveals that the minimum and maximum timescales are centered on 4 (Group 1a) and 10–11 (Group 1b) months, while the limited dataset of Group 2 peaks at 1.7–1.8 year (see Figs 10 and A.21). Importantly, 68% of the overall minimum timescales (Group 1 + Group 2) fall within <1 year, and 95% within 2 years (Fig. 10). The maximum timescales yield peak values comparable to the minimum ones (see Fig. A.21), with 68% of the maximum timescales falling within 1 year (95% within 2.2 years).

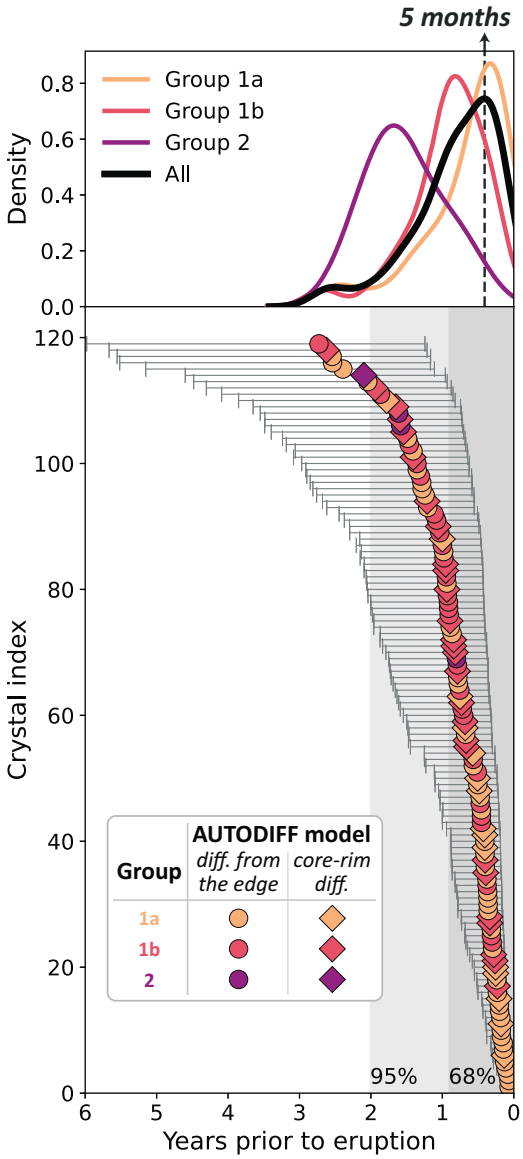

Figure 10. Minimum timescales (determined in dry conditions, at 1139°C for Group 1a and 1b, and 1142°C for Group 2) inferred from Fe–Mg diffusion chronometry in 119 olivine crystals plotted against their crystal index, i.e. their rank when sorting timescales from smallest to largest (e.g. Hartley *et al.*, 2016; Pankhurst *et al.*, 2018; Rasmussen *et al.*, 2018). Colour variations denote the different groups: 1a, 1b, and 2. Symbols represent the AUTODIFF model from which these timescales were obtained: circles indicate diffusion (diff.) from the edge (assuming no growth, only diffusion); diamonds assume that rim growth occurred rapidly enough to separate the core–rim interface from the melt before any significant diffusion. A KDE is plotted at the top, reflecting the density of timescales obtained for each group.

Discussion

The CM eruption was previously interpreted by Harris & Russell (2022) as the result of the syn-eruptive mixing of two distinct crustal magma reservoirs, based on differences in erupted phenocryst assemblages. These assemblages include OP and OPA glomerocrysts, each reflecting unique storage conditions. Building on this framework, our work refines this two-reservoir model by directly linking our identified olivine populations to specific storage zones. By integrating textural and chemical evidence, we further reconstruct how these populations interacted within a shared reservoir and ultimately fed the eruption. Pre-eruptive mixing followed by fractional crystallisation left chemical and textural signatures in the olivine populations, providing critical insights into the magmatic processes and timing leading up to the eruption. This newly proposed scenario is depicted in Fig. 11.

Storage of OP and OPA magmas

The OP reservoir and Group 1 olivine

Group 1 crystals, comprising both subgroups 1a and 1b, are identified based on their chemical and textural characteristics, including the presence or absence and spatial distribution of spinel and sulphide inclusions. Indeed, the subgroups share similar features,

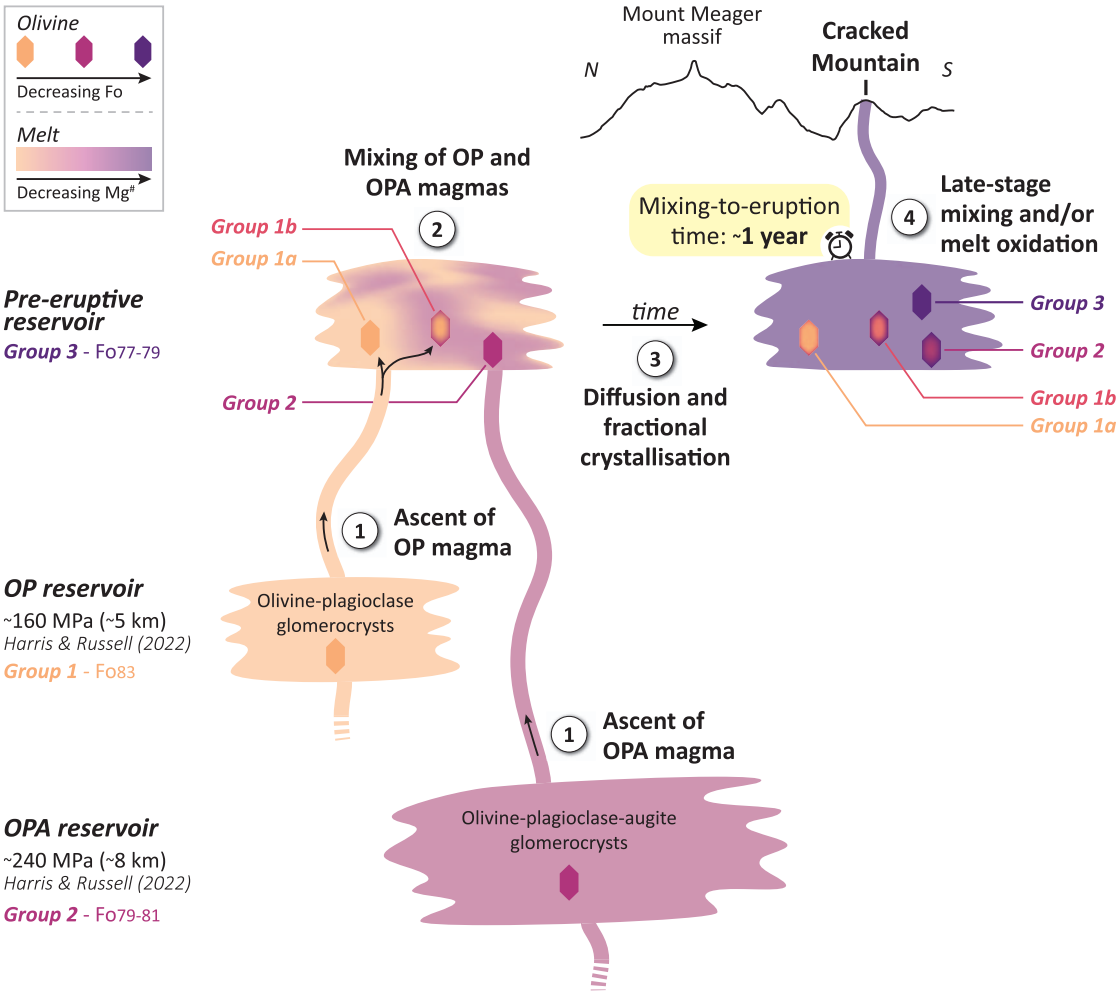

Figure 11. Schematic cross-section of the CM transcrustal magmatic system based on the three populations of olivine phenocrysts identified. (1) The OP magma (comprising olivine–plagioclase glomerocrysts) and the OPA magma (comprising olivine–plagioclase–augite glomerocrysts) ascended through the crust, possibly related to magma recharge and/or glacial unloading (Harris & Russell, 2022). (2) During heterogeneous mixing of OP and OPA magmas in the pre-eruptive reservoir, Group 1b crystals encountered the more evolved OPA melt early, promoting rapid rim growth, whereas Group 1a crystals remained longer in OP melt; Group 2 crystals largely remained within their host OPA melt. (3) From mixing through to diffusion and fractional crystallisation, both Group 1 (associated with OP origin) and Group 2 (associated with OPA origin) developed rims with more evolved compositions, forming normal zoning. Simultaneously, a later stage of Group 3 crystals formed, this time with a skeletal texture. Applying Fe–Mg diffusion chronometry to the zoned olivine crystals, we estimate that the Group 1 and 2 olivine phenocrysts co-existed in the same evolving, hybrid melt for ~1 year. (4) Subsequently, a late-stage mixing event and/or oxidation of the melt likely triggered the eruption, indicated by a slight reverse zoning observed on the outermost rims of some of the olivine crystals.

including rare spinel inclusions, of the same size and composition, exclusively located within olivine rims or embayments (e.g. Figs 4g, 8a, and 9). Globular sulphide inclusions are also present in limited numbers across both subgroups (see Appendix J), suggesting their host melt reached sulphide saturation at some point in their evolution. The two subgroups also show a continuum in zoning patterns and core compositions, with Group 1a being slightly more forsterite-rich (~Fo_{83} core) than Group 1b (~Fo_{82} core), and all Group 1 compositions plotting within the OP field (Harris & Russell, 2022; Fig. 5). The comparatively less Fo-rich compositions and more pronounced zoning of Group 1b, relative to Group 1a, could be attributed to various factors such as crystal orientation effects and/or depth of sectioning, with Group 1b reflecting more superficial sections (i.e. not cutting through the crystal's core) than Group 1a. However, this last hypothesis is less likely, given that the distribution of the most superficial sections is balanced between the two subgroups (28% and 33% for Groups 1a and 1b, respectively). Alternatively, these differences can be readily explained by Group 1b crystals interacting with a more evolved melt at an earlier stage than Group 1a, as suggested by their broader diffusion widths (Figs 6a, b and 8a) and associated longer timescales (Fig. 10). Despite this temporal offset, both subgroups are inferred to have formed within the same reservoir under conditions consistent with the OP reservoir, at depths shallower than 7 km (<200 MPa; Harris & Russell, 2022; Fig. 11).

The OPA reservoir and Group 2 olivine

The Group 2 olivine phenocrysts exhibit distinct characteristics that necessitate crystallisation under different conditions than those of Group 1 (OP): (1) abundant spinel inclusions in their cores, rims, and embayments; (2) the absence of sulphide inclusions; and (3) lower Fo and NiO contents coupled with weak normal zoning (Figs 5 and 8a), a feature not attributable to superficial sectioning (only 21% of crystals are shallowly cut). The crystallisation of Group 2 olivine within the OPA reservoir is supported by several lines of evidence. First, Group 2 olivine cores plot within the OPA compositional field defined by Harris & Russell (2022) (Fig. 5). Second, OPA glomerocrysts are rare in thin section, consistent

with the limited abundance of Group 2 olivine phenocrysts in our dataset. Finally, spinel inclusions are ubiquitous in OPA glomerocrysts (occurring in olivine, clinopyroxene, and, to a lesser extent, plagioclase), closely matching the high abundance of spinel inclusions observed in Group 2 olivine. Collectively, these observations suggest that Group 2 olivine crystallised within the OPA reservoir at depths of 7–8 km (200–250 MPa; Harris & Russell, 2022).

Ascent of OP and OPA magmas

The coexistence of Group 1 and Group 2 olivine populations across all samples (Fig. 3), regardless of their classification as OP or OPA by Harris & Russell (2022) (e.g. *AW-15-163* and *MH-19-047* as OP; *MH-19-032* as OPA), suggests that the OP and OPA magmas interacted during their ascent. However, the relative dominance of one population over the other within individual samples (Fig. 3) indicates that these populations were not homogeneously mixed prior to eruption.

Group 1 crystals display textural and chemical evidence of past dissolution events, including rounded corners (19% of the Group 1 crystals), cuspate margins (14% of Group 1; Figs 4a, c and 6), embayments (81% of Group 1; Fig. 4a–c), and internal phosphorus signatures that reveal truncated primary and secondary branches (i.e. the olivine 'skeleton'; see Fig. 8a and d for Group 1a). These features suggest that some crystals underwent 'petrological cannibalism', likely due to prior interaction(s) with a hotter recharge magma (Cashman & Blundy, 2013). Indeed, similar textures were documented in olivine phenocrysts of comparable compositions (i.e. ~Fo_{83} and 0.15–0.28 wt % NiO) from the nearby *Lillooet Glacier* eruption. Their short- and long-wavelength cuspate margins were attributed to the injection of a hotter and basaltic magma (Aufrère *et al.*, 2024), with cusp wavelength increasing as the magma undergoes cooling (Thornber & Huebner, 1985). In contrast, the rounded corners and short-wavelength cuspate margins observed here imply resorption within a more silica-enriched liquid (~52 wt % SiO_2), with the development of cusps occurring as temperature decreases (Thornber & Huebner, 1985). Altogether, this repeated record of resorbed Fo_{83} olivine phenocrysts across eruptions 25 km (Fig. 1b) and ~400 ka apart (Wilson & Russell, 2017; Harris *et al.*, 2022; Harris & Russell, 2022) suggests a stable mafic magma source that produced and later reworked these crystals through renewed inputs.

Whereas OP ascent involved magma recharge and olivine partial resorption, OPA (Group 2) olivine crystals lack such features: they show neither cuspate margins nor truncated skeletal branches, indicating that ascent was not triggered by magma recharge. Instead, OPA ascent may have been driven by external factors, such as glacial unloading (Wilson & Russell, 2020). Indeed, Harris & Russell (2022) and Harris *et al.* (2022) noted that retreat of the Cordilleran Ice Sheet in SW British Columbia coincides with the CM eruption age, suggesting that unloading may have reduced lithostatic pressure, thus facilitating magma ascent. Deglaciation may therefore have directly enabled OPA magma ascent, while also playing a role in facilitating recharge of the OP reservoir (Step 1 in Fig. 11).

Pre-eruptive mixing, diffusion, and crystallisation

The OP and OPA magmas eventually stalled in a common pre-eruptive magma reservoir, where heterogenous mixing took place (Step 2 in Fig. 11), contributing to the observed olivine populations in our samples (Fig. 3).

Interaction of OP and OPA crystals in a common reservoir

Compared to Group 1a, Group 1b crystals show evidence of earlier interaction with a more evolved melt, as reflected in their overall longer timescales (Fig. 10). They also more commonly exhibit features of rapid rim growth, including skeletal morphologies (Figs 4f, h and 8) and step-like diffusion profiles in more than half of the crystals (Fig. 6h). Group 1b crystals therefore likely came into direct contact with the more evolved OPA melt early in the mixing process, promoting rapid rim growth. In contrast, Group 1a crystals appear to have remained within portions of the OP melt for longer periods, allowing for a more gradual interaction with more evolved mixed melts. Similarly, the Group 2 crystals likely mostly stayed in their host OPA melt rather than entering in direct contact with the OP melt, as Group 2 olivine crystals do not display disequilibrium textures that would suggest mixing with the OP magma early on.

Diffusion in Groups 1 and 2 olivine crystals began shortly after mixing of the OP and OPA magmas (and in some cases after rim crystallisation) and continued as the mixed magma evolved. This stage is recorded by compositional gradients across crystal rims and by diffusion profiles modelled in both crystal groups (e.g. Fig. 6).

Late-stage crystallisation of Group 3 olivine

As the system evolved, Group 3 olivine phenocrysts crystallised (Step 3 in Fig. 11), at temperatures ranging from 1137 ± 29 to 1144 ± 44°C (Table 2). These crystals are characterised by the most Fe-rich core compositions ($Fo_{77–78}$) in equilibrium with the pre-eruptive melt ($Mg^{\#}_{51}$; Fig. A.22 in Appendix I), most do not display any inner zoning (e.g. Fig. 8), and a significant number of these crystals are skeletal (Figs 4p, 5, and 8). Interestingly, their Fo contents overlap entirely with skeletal olivine microphenocrysts that crystallised within the pre-eruptive magma reservoir, which fed the nearby (but more recent) *Lillooet Glacier* eruption ($Fo_{76–79}$; Aufrère *et al.*, 2024), indicating that the same pre-eruptive melt compositions were repeatedly established within the MMVC magmatic system. The prevalence of skeletal textures, together with the limited core–rim compositional variation in Group 2 crystals, indicates that fractional crystallisation in the pre-eruptive reservoir was minimal (Step 3 in Fig. 11).

Diffusion timescales and eruption primers

Diffusion modelling of Groups 1 and 2 olivine crystals at pre-eruptive temperatures of 1132 ± 29 to 1142 ± 44°C (Table 2) yields mixing-to-eruption timescales centred on 5 months, with most (68%) falling within <1 year and extending to 2 years (95%; Fig. 10). This spread may be explained by gradual contact of the OP crystals with the OPA magma; some crystals may also have been shielded within crystal clots during early stages of mixing, thereby recording shorter diffusion durations. These timescales are comparable, though slightly longer, than the 1–3 months pre-eruptive residence time previously constrained for the nearby *Lillooet Glacier* eruption (Aufrère *et al.*, 2024). Comparable timescales have also been documented at the nearest volcanic field where diffusion chronometry has been applied, Mt. Baker (Washington, USA; Fig. 1a). There, mafic recharge and/or thermal events appear to have primed multiple eruptions, with timescales derived from Fe–Mg interdiffusion in clinopyroxene and Mg and Sr diffusion in plagioclase predominantly spanning within 1 year, extending to several years (Cunningham, 2024; Yoder, 2024).

Late-stage mixing and/or melt oxidation

Approximately 50% of the observed crystals (mostly Group 2 and 3) exhibit either minor reverse zoning, characterised by up to a 1.3 mol % increase in Fo, or maintain a plateau at their outermost rims with respect to their Fo compositional profiles. Notably, this reverse zoning or plateau is not consistently mirrored by NiO, which typically either plateaus (Fig. 7f) or decreases slightly (Figs 6f and 7e).

The observed Fo–NiO decoupling likely reflects diffusive re-equilibration following rapid olivine rim growth (Lynn *et al.*, 2017). Since Fe–Mg diffuses faster than Ni in olivine (Chakraborty, 2010 and references therein), Fo responds more readily to diffusive modification than NiO, producing small Fo reversals or plateaus at the rims alongside relatively constant or slightly decreasing NiO. The very limited extent of Fo diffusion precludes quantitative timescale modelling (see section Results) and indicates that this event occurred shortly prior to eruption.

Several late-stage processes could have triggered such rapid rim growth. One possibility is interaction with a more primitive melt (Lynn *et al.*, 2017), either through recharge or self-mixing, which can rapidly modify melt composition and redox conditions. An alternative (though not mutually exclusive) trigger is late-stage oxidation of the resident magma. Indeed, increases in fO_2 conditions have been linked to similar (or larger) Fo enrichments at olivine outer rims in kimberlitic and basaltic systems (Landi *et al.*, 2006; Howarth & Gross, 2019). Oxidation promotes Fe^{3+} formation at the expense of Fe^{2+}, reducing Fe^{2+} availability for olivine, and driving rims towards higher Fo (hence the reverse zoning). Evidence for an increase in oxidation state is further provided by the final spinel oxides to crystallise, located in olivine embayments or along crystal edges and characterised by the lowest $Mg^{\#}$ content, as they exhibit greater enrichment in Fe^{3+} and Ti compared to those situated in the Group 2 cores or the rims of Groups 1 and 2 (Fig. 9). Since the samples studied here were quenched upon eruption, it is unlikely that the inferred increase in fO_2 reflects the addition of glacier meltwater to the CM lava. Instead, a possible explanation may involve an interaction with Mount Meager's hydrothermal system in the upper crust, though its extent is not precisely characterised beneath CM (Hanneson & Unsworth, 2023).

Regardless of the exact late-stage event—whether mixing with a more primitive melt, oxidation of the resident magma, or both—these processes may have acted as the eruption trigger by modifying melt composition and/or redox conditions in the shallow pre-eruptive reservoir (Step 4 in Fig. 11).

Monitoring and hazard implications

This study, combined with the work of Aufrère *et al.* (2024), demonstrates through two eruptions 25 km (Fig. 1b) and ~400 ka apart (Wilson & Russell, 2017; Harris *et al.*, 2022; Harris & Russell, 2022) that mafic eruptions at the MMVC can be preceded by short timescales. Despite this, Mount Meager—one of Canada's two very high-threat volcanoes—remains monitored only at a level commensurate with a very low-threat edifice (Kelman & Wilson, 2024). While this ranking largely reflects its recent, explosive felsic history (i.e. the VEI 4, 2360 years BP eruption) and active hydrothermal system, renewed mafic volcanism also warrants consideration. Indeed, effusive mafic eruptions are frequent across the GVB, and their vents are commonly situated at high elevations above major drainages and transportation corridors. In such a setting, low-viscosity lava flows can be readily channelised into valleys, allowing them to travel rapidly for long distances and interact with infrastructure. Pleistocene examples include the Cheakamus (26 km long; Borch *et al.*, 2023) and Elaho Valley (~20 km long; Harris *et al.*, 2023) lavas, which illustrate that flows can extend well beyond vent areas. In the absence of valley glaciers today, mafic flows could travel even further, with cascading impacts such as river damming and secondary flooding. This hazard, combined with short pre-eruptive timescales, is compounded by projected population growth and infrastructure expansion in SW British Columbia, where communities such as those in the Squamish–Lillooet Regional District have grown by >40% since 2006 (Statistics Canada, 2023). Thus, while the most catastrophic scenarios at MMVC remain associated with felsic volcanism (Warwick *et al.*, 2022), even modest mafic eruptions could have regionally significant consequences. Improving monitoring capacity would therefore provide critical lead time should unrest signal the onset of either mafic or felsic activity.

Conclusion

By integrating petrological and geochemical evidence from olivine phenocrysts, we shed new light on the magmatic processes that preceded the CM eruption. Our results, building on the framework of Harris & Russell (2022), show the existence and pre-eruptive interaction of, at least, two magma reservoirs: OPA and OP.

Initially, the OPA magma resided at a depth of ~8 km (~240 MPa) and contained OPA glomerocrysts. Group 2 olivine crystals from this magma are characterised by co-crystallisation with augite, $Fo_{79–81}$ compositions, abundant spinel inclusions, and the absence of sulphide inclusions. The OP reservoir was located closer to the surface, at ~5 km depth (~160 MPa), and hosted Group 1 olivine crystals, which are more Mg-rich than those from the OPA magma ($Fo_{\sim 83}$), lack spinel inclusions, and contain rare sulphide inclusions. The OP and OPA magmas subsequently ascended to shallower depths (Step 1 in Fig. 11), potentially driven by magma recharge and/or glacial unloading (Harris & Russell, 2022), where they interacted in a pre-eruptive reservoir (Step 2 in Fig. 11). While Group 1b crystals underwent rapid rim growth after early contact with the more evolved OPA melt, Group 1a crystals remained longer in OP melt, recording more gradual interaction with mixed compositions. Group 2 crystals, by contrast, largely remained within their host OPA melt. Mixing in this reservoir was efficient but incomplete, as Group 1 and Group 2 olivine phenocrysts are found across all samples but in varying proportions.

Along with limited fractional crystallisation, this triggered diffusion towards equilibrium at the crystal rims, sometimes preceded by rim growth and spinel inclusion in the Group 1 rims (Step 3 in Fig. 11). At this stage, both Group 1 (OP) and Group 2 (OPA) crystals became normally zoned: Group 1 due to their exposure to the evolved melt, and Group 2 due to limited fractional crystallisation. Simultaneously, new, more Fe-rich Group 3 phenocrysts ($Fo_{77–78}$) with skeletal features crystallised in equilibrium with the pre-eruptive magma ($Mg^{\#}_{51}$, consistent with the glassy groundmass composition). Diffusion modelling across the zoned olivine crystals indicates mixing-to-eruption timescales predominantly within <1 year (68%) and extending up to 2 years (95%).

Finally, late-stage mixing and/or oxidation of the melt (Step 4 in Fig. 11) is evidenced by Fo-NiO decoupling on the outermost rims of ~50% of the studied olivine crystals, with minor Fo reverse zoning or plateauing and NiO either plateauing or slightly decreasing. Additionally, the most recently crystallised spinel oxides, located on rims and within embayments, are enriched in Fe^{3+} and Ti, further supporting late-stage oxidation. This oxidation may have

been driven by interaction with Mount Meager's hydrothermal system; such destabilisation of the system might have triggered the eruption.

These findings complement earlier work on the *Lillooet Glacier* eruption at MMVC (Aufrère *et al.*, 2024), underscoring the relatively short pre-eruptive magmatic timescales of the MMVC and the need for monitoring systems to be implemented. Our results also highlight the presence of a recurrent magmatic supply system, which produces consistent olivine compositions, both as entrained crystals and as autocrysts crystallised within a pre-eruptive magma reservoir.

Acknowledgements

We respectfully acknowledge that the area that inspired this research is within the traditional unceded territories of the Líl̓wat First Nation. We thank A. Wilson and M. Harris (formerly of University of British Columbia) for access to the UBC CM samples. We would like to thank C. Névado (Université de Montpellier) for his help preparing the grain-mounts, F. Barou (Université de Montpellier) for his assistance with the EBSD, E. Voyer (Laboratoire Magma et Volcans) with the SEM, and J.-L. Devidal (Laboratoire Magma et Volcans) and A. von der Handt (University of British Columbia) with the EPMAs. Lastly, we thank M. Harris, K. Lynn, and two anonymous reviewers for their thoughtful comments that greatly improved this manuscript.

Supplementary data

Supplementary data are available at *Journal of Petrology* online.

Data availability

Analytical data for this study is available in the online supplementary material, as well as in the EarthChem.org database at https://doi.org/10.60520/IEDA/113665 (Aufrère & Williams-Jones, 2025). The updated version (v2) of the Python *Greyscale-to-Fo* converter code is available via the Zenodo.org database at https://doi.org/10.5281/zenodo.14545387 (Aufrère *et al.*, 2025).

Conflict of interests

No conflict of interest is declared.

Funding

This research was supported by Natural Sciences and Engineering Research Council of Canada Discovery grants (RGPIN-2016-03953, RGPIN-2023-04284) to G.W.J.

REFERENCES

Andrews, G. D. M., Russell, J. K. & Stewart, M. L. (2014). The history and dynamics of a welded pyroclastic dam and its failure. *Bulletin of Volcanology* **76**(4), 1–16. https://doi.org/10.1007/s00445-014-0811-0.

Aufrère, S. M., Anzieta, J. & Williams-Jones, G. (2025). Greyscale-Fo analysis tools for olivine diffusion chronometry. https://doi.org/10.5281/zenodo.14545387.

Aufrère, S. M. and Williams-Jones, G. (2025). Glass, olivine and spinel analyses from the Cracked Mountain basalts, Mount Meager Volcanic Complex (British Columbia, Canada), *Version* **1**.0 https://doi.org/10.60520/IEDA/113665

Aufrère, S. M., Williams-Jones, G., Moune, S., Morgan, D. J., Vigouroux, N. & Russell, J. K. (2024). Olivine time-capsules constrain the pre-eruptive history of Holocene basalts, Mount Meager volcanic complex, British Columbia, Canada. *Journal of Petrology* **65**(9). https://doi.org/10.1093/petrology/egae089.

Bachmann, F., Hielscher, R. & Andrews, G. D. M. (2010). Texture analysis with MTEX – free and open source software toolbox. *Solid State Phenomena* **160**, 63–68. https://doi.org/10.4028/www.scientific.net/SSP.160.63.

Beattie, P. (1993). Olivine-melt and orthopyroxene-melt equilibria. *Contributions to Mineralogy and Petrology* **115**, 103–111. https://doi.org/10.1007/BF00712982.

Bell, S., Morgan, D., Joy, K., Pernet-Fisher, J. & Hartley, M. (2023). Determining the thermal histories of Apollo 15 mare basalts using diffusion modelling in olivine. *Geochimica et Cosmochimica Acta* **357**, 77–91. https://doi.org/10.1016/j.gca.2023.08.009.

Borch, A., Russell, J. K. & Barendregt, R. (2023). Cheakamus basalt lavas, British Columbia: a Pleistocene record of rapid, continuous eruption within a mountainous drainage system. *Canadian Journal of Earth Sciences* **60**(11), 1544–1572. https://doi.org/10.1139/cjes-2023-0004.

Borisov, A., Behrens, H. & Holtz, F. (2018). Ferric/ferrous ratio in silicate melts: a new model for 1 atm data with special emphasis on the effects of melt composition. *Contributions to Mineralogy and Petrology* **173**, 1–15. https://doi.org/10.1007/s00410-018-1524-8.

Cashman, K. & Blundy, J. (2013). Petrological cannibalism: the chemical and textural consequences of incremental magma body growth. *Contributions to Mineralogy and Petrology* **166**(3), 703–729. https://doi.org/10.1007/s00410-013-0895-0.

Chakraborty, S. (2010). Diffusion coefficients in olivine, wadsleyite and ringwoodite. *Reviews in Mineralogy and Geochemistry* **72**(1), 603–639. https://doi.org/10.2138/rmg.2010.72.13.

Chakraborty, S. & Dohmen, R. (2022). Diffusion chronometry of volcanic rocks: looking backward and forward. *Bulletin of Volcanology* **84**(6), 57. https://doi.org/10.1007/s00445-022-01565-5.

Clance, J., Shaffer, J., Cable, M., Stenner, C., Williams-Jones, G., Szynkiewicz, A., Paton, M., Graham, H., Vinnes, O. & Mikucki, J. (2024). Biogeochemistry of the rare sulfidic glaciovolcanic cave system on Mount Meager, British Columbia, Canada. *Frontiers in Geochemistry* **2**, 1410338. https://doi.org/10.3389/fgeoc.2024.1410338.

Costa, F. & Morgan, D. (2010) Time constraints from chemical equilibration in magmatic crystals. In: Dosseto A., Turner S. P. & Van Orman J. A. (eds) *Timescales of Magmatic Processes: From Core to Atmosphere*. Hoboken, New Jersey, USA: Wiley-Blackwell, pp.125–159.

Couperthwaite, F. K., Morgan, D. J., Pankhurst, M. J., Lee, P. D. & Day, J. M. (2021). Reducing epistemic and model uncertainty in ionic inter-diffusion chronology: a 3D observation and dynamic modeling approach using olivine from Piton de la Fournaise, *La Réunion*. *American Mineralogist* **106**(3), 481–494. https://doi.org/10.2138/am-2021-7296CCBY.

Couperthwaite, F. K., Thordarson, T., Morgan, D. J., Harvey, J. & Wilson, M. (2020). Diffusion timescales of magmatic processes in the Moinui lava eruption at Mauna Loa, Hawai'i, as inferred from bimodal olivine populations. *Journal of Petrology* **61**(7). https://doi.org/10.1093/petrology/egaa058.

Cunningham, D. (2024). *Timescales of Magma Storage and the Pre-eruptive History for the Most Recent Lava Flow at Mount Baker (Koma Kulshan)*, WA. Master's Thesis, Central Washington University, https://digitalcommons.cwu.edu/etd/1936

Dohmen, R., Becker, H.-W. & Chakraborty, S. (2007). Fe-Mg diffusion in olivine I: experimental determination between 700 and 1,200°C

as a function of composition, crystal orientation and oxygen fugacity. *Physics and Chemistry of Minerals* **34**(6), 389–407. https://doi.org/10.1007/S00269-007-0157-7.

Dohmen, R. & Chakraborty, S. (2007a). Fe-Mg diffusion in olivine II: point defect chemistry, change of diffusion mechanisms and a model for calculation of diffusion coefficients in natural olivine. *Physics and Chemistry of Minerals* **34**(6), 409–430. https://doi.org/10.1007/S00269-007-0158-6.

Dohmen, R. & Chakraborty, S. (2007b). Fe-Mg diffusion in olivine II: point defect chemistry, change of diffusion mechanisms and a model for calculation of diffusion coefficients in natural olivine. *Physics and Chemistry of Minerals* **34**(8), 597–598. https://doi.org/10.1007/s00269-007-0185-3.

Dungan, M. A., Long, P. E. & Rhodes, J. (1978). Magma mixing at mid-ocean ridges: evidence from legs 45 and 46-DSDP. *Geophysical Research Letters* **5**(6), 423–425. https://doi.org/10.1029/GL005I006P00423.

Frost, B. R. (1991) Chapter 1. Introduction to oxygen fugacity and its petrologic importance. In: Lindsley D. H. (ed) *Oxide Minerals: Petrologic and Magnetic Significance*. Berlin, Boston: De Gruyter, pp.1–10.

Gualda, G. A. & Ghiorso, M. S. (2015). MELTS_Excel: a Microsoft Excel-based MELTS interface for research and teaching of magma properties and evolution. *Geochemistry, Geophysics, Geosystems* **16**(1), 315–324. https://doi.org/10.1002/2014GC005545.

Gualda, G. A. R., Ghiorso, M. S., Lemons, R. V. & Carley, T. L. (2012). Rhyolite-MELTS: a modified calibration of MELTS optimized for silica-rich, fluid-bearing magmatic systems. *Journal of Petrology* **53**(5), 875–890. https://doi.org/10.1093/petrology/egr080.

Hanneson, C. & Unsworth, M. J. (2023). Magnetotelluric imaging of the magmatic and geothermal systems beneath Mount Meager, southwestern Canada. *Canadian Journal of Earth Sciences* **60**(10), 1385–1403. https://doi.org/10.1139/cjes-2022-0136.

Harris, M. A. & Russell, J. K. (2022). Polymagmatic glaciovolcanism: Cracked Mountain tuya, Canadian Cascades. *Frontiers in Earth Science* **10**. https://doi.org/10.3389/feart.2022.859794.

Harris, M. A., Russell, J. K., Barendregt, R., Porritt, L. A. & Wilson, A. (2022). Explosive glaciovolcanism at Cracked Mountain Volcano, Garibaldi Volcanic Belt, Canada. *Journal of Volcanology and Geothermal Research* **423**, 107477. https://doi.org/10.1016/j.jvolgeores.2022.107477.

Harris, M. A., Russell, J. K., Wilson, A. & Jicha, B. (2023). A 500 ka record of volcanism and paleoenvironment in the northern Garibaldi Volcanic Belt, British Columbia. *Canadian Journal of Earth Sciences* **60**(4), 401–421. https://doi.org/10.1139/cjes-2022-0101.

Hartley, M. E., Morgan, D. J., Maclennan, J., Edmonds, M. & Thordarson, T. (2016). Tracking timescales of short-term precursors to large basaltic fissure eruptions through Fe–Mg diffusion in olivine. *Earth and Planetary Science Letters* **439**, 58–70. https://doi.org/10.1016/j.epsl.2016.01.018.

Hickson, C. J., Russell, J. K. & Stasiuk, M. V. (1999). Volcanology of the 2350 B.P. eruption of Mount Meager volcanic complex, British Columbia, Canada: implications for hazards from eruptions in topographically complex terrain. *Bulletin of Volcanology* **60**(7), 489–507. https://doi.org/10.1007/s004450050247.

Hildreth, W. (2007) *Quaternary mMgmatism in the Cascades: Geologic Perspectives*. US Geological Survey.

Howarth, G. H. & Gross, J. (2019). Diffusion-controlled and concentric growth zoning revealed by phosphorous in olivine from rapidly ascending kimberlite magma, Benfontein, South Africa. *Geochimica et Cosmochimica Acta* **266**, 292–306. https://doi.org/10.1016/j.gca.2019.08.006.

Huebner, J. S. & Sato, M. (1970). The oxygen fugacity-temperature relationships of manganese oxide and nickel oxide buffers. *American Mineralogist* **55**(5–6), 934–952.

Iacovino, K. (2022). Calculate fO2 buffer. https://doi.org/10.5281/zenodo.7387196.

Iddings, J. P. (1892). On the crystallization of igneous rocks. *Bulletin of the Philosophical Society of Washington* **11**, 71–112.

Joy, D. C. (1974) Electron channeling patterns in the SEM. In: Holt D. B., Muir M. D., Boswarva I. M. & Grant P. R. (eds) *Quantitative Scanning Electron Microscopy*. New York: Academic Press.

Kahl, M., Morgan, D. J., Thornber, C., Walshaw, R., Lynn, K. J. & Trusdell, F. A. (2023). Dynamics of magma mixing and magma mobilisation beneath Mauna Loa—insights from the 1950 AD southwest rift zone eruption. *Bulletin of Volcanology* **85**(12), 75. https://doi.org/10.1007/s00445-023-01680-x.

Kelley, K. A. & Cottrell, E. (2009). Water and the oxidation state of subduction zone magmas. *Science* **325**(5940), 605–607. https://doi.org/10.1126/science.1174156.

Kelman, M. C. & Wilson, A. M. (2024). Assessing the relative threats from Canadian volcanoes. *Canadian Journal of Earth Sciences* **61**(3), 408–430. https://doi.org/10.1139/cjes-2023-0074.

Landi, P., Francalanci, L., Pompilio, M., Rosi, M., Corsaro, R., Petrone, C., Nardini, I. & Miraglia, L. (2006). The December 2002–July 2003 effusive event at Stromboli volcano, Italy: insights into the shallow plumbing system by petrochemical studies. *Journal of Volcanology and Geothermal Research* **155**(3–4), 263–284. https://doi.org/10.1016/j.jvolgeores.2006.03.032.

Le Bas, M. J., Le Maitre, R. W., Streckeisen, A., Zanettin, B. & IUGS Subcommission on the Systematics of Igneous Rocks (1986). A chemical classification of volcanic rocks based on the total alkali-silica diagram. *Journal of Petrology* **27**(3), 745–750. https://doi.org/10.1093/petrology/27.3.745.

Leiter, S., Russell, J. K., Heap, M. J., Barendregt, R. W., Wilson, S. & Edwards, B. (2024). Distribution, intensity, and timing of palagonitization in glaciovolcanic deposits, Cracked Mountain volcano, Canada. *Bulletin of Volcanology* **86**, 32. https://doi.org/10.1007/s00445-024-01724-w.

Lloyd, G. E., Ferguson, C. C. & Law, R. D. (1987). Discriminatory petrofabric analysis of quartz rocks using SEM electron channelling. *Tectonophysics* **135**(1–3), 243–249. https://doi.org/10.1016/0040-1951(87)90165-X.

Lynn, K. J., Downs, D. T., Trusdell, F. A., Wieser, P. E., Rangel, B., McDade, B., Hotovec-Ellis, A. J., Bennington, N., Anderson, K. R., Ruth, D. C., DeVitre, C., Ellis, A. P., Nadeau, P. A., Clor, L., Kelly, P., Dotray, P. J. & Chang, J. C. (2024). Triggering the 2022 eruption of Mauna Loa. *Nature Communications* **15**, 9451. https://doi.org/10.1038/s41467-024-52881-7.

Lynn, K. J., Garcia, M. O., Shea, T., Costa, F. & Swanson, D. A. (2017). Timescales of mixing and storage for Keanakāko'i tephra magmas (1500–1820 C.E.), Kīlauea volcano, Hawai'i. *Contributions to Mineralogy and Petrology* **172**(8), 76. https://doi.org/10.1007/s00410-017-1395-4.

Lynn, K. J., Shea, T. & Garcia, M. O. (2017). Nickel variability in Hawaiian olivine: evaluating the relative contributions from mantle and crustal processes. *American Mineralogist* **102**(3), 507–518. https://doi.org/10.2138/am-2017-5763.

Martin, V. M., Morgan, D. J., Jerram, D. A., Caddick, M. J., Prior, D. J. & Davidson, J. P. (2008). Bang! Month-scale eruption triggering at Santorini volcano. *Science* **321**(5893), 1178. https://doi.org/10.1126/science.1159584.

Metcalfe, A., Moune, S., Komorowski, J.-C., Kilgour, G., Jessop, D. E., Moretti, R. & Legendre, Y. (2021). Magmatic processes at La Soufrière de Guadeloupe: insights from crystal studies and

diffusion timescales for eruption onset. *Frontiers in Earth Science* **9**, 617294. https://doi.org/10.3389/feart.2021.617294.

Michol, K. A., Russell, J. K. & Andrews, G. D. M. (2008). Welded block and ash flow deposits from Mount Meager, British Columbia, Canada. *Journal of Volcanology and Geothermal Research* **169**(3–4), 121–144. https://doi.org/10.1016/j.jvolgeores.2007.08.010.

Morgan, D., Blake, S., Rogers, N., DeVivo, B., Rolandi, G., Macdonald, R. & Hawkesworth, C. (2004). Time scales of crystal residence and magma chamber volume from modelling of diffusion profiles in phenocrysts: Vesuvius 1944. *Earth and Planetary Science Letters* **222**(3), 933–946. https://doi.org/10.1016/j.epsl.2004.03.030.

Mourey, A. J., Shea, T. & Hammer, J. E. (2023). Preservation of magma recharge signatures in Kīlauea olivine during protracted storage. *Journal of Geophysical Research: Solid Earth* **128**(1), e2022JB025523. https://doi.org/10.1029/2022JB025523.

Newhall, C. G. & Self, S. (1982). The volcanic explosivity index (VEI): an estimate of explosive magnitude for historical volcanism. *Journal of Geophysical Research* **87**, 1231–1238. https://doi.org/10.1016/j.epsl.2020.116500.

Pankhurst, M. J., Morgan, D. J., Thordarson, T. & Loughlin, S. C. (2018). Magmatic crystal records in time, space, and process, causatively linked with volcanic unrest. *Earth and Planetary Science Letters* **493**, 231–241. https://doi.org/10.1016/j.epsl.2018.04.025.

Petrone, C., Bugatti, G., Braschi, E. & Tommasini, S. (2016). Pre-eruptive magmatic processes re-timed using a non-isothermal approach to magma chamber dynamics. *Nature Communications* **7**, 12946. https://doi.org/10.1038/ncomms12946.

Prior, D. J., Boyle, A. P., Brenker, F., Cheadle, M. C., Day, A., Lopez, G., Peruzzo, L., Potts, G. J., Reddy, S., Spiess, R., Timms, N. E., Trimby, P., Wheeler, J. & Zetterström, L. (1999). The application of electron backscatter diffraction and orientation contrast imaging in the SEM to textural problems in rocks. *American Mineralogist* **84**(11–12), 1741–1759. https://doi.org/10.2138/am-1999-11-1204.

Prior, D. J., Trimby, P. W., Weber, U. D. & Dingley, D. J. (1996). Orientation contrast imaging of microstructures in rocks using forescatter detectors in the scanning electron microscope. *Mineralogical Magazine* **60**(403), 859–869. https://doi.org/10.1180/minmag.1996.060.403.01.

Pu, X., Lange, R. A. & Moore, G. (2017). A comparison of olivine-melt thermometers based on D_{Mg} and D_{Ni}: the effects of melt composition, temperature, and pressure with applications to MORBs and hydrous arc basalts. *American Mineralogist* **102**(4), 750–765. https://doi.org/10.2138/am-2017-5879.

Pu, X., Moore, G. M., Lange, R. A., Touran, J. P. & Gagnon, J. E. (2021). Experimental evaluation of a new H_2O-independent thermometer based on olivine-melt Ni partitioning at crustal pressure. *American Mineralogist* **106**(2), 235–250. https://doi.org/10.2138/am-2020-7014.

Putirka, K. D. (2008). Thermometers and barometers for volcanic systems. *Reviews in Mineralogy and Geochemistry* **69**(1), 61–120. https://doi.org/10.2138/rmg.2008.69.3.

Putirka, K. D., Perfit, M., Ryerson, F. & Jackson, M. G. (2007). Ambient and excess mantle temperatures, olivine thermometry, and active vs. passive upwelling. *Chemical Geology* **241**(3–4), 177–206. https://doi.org/10.1016/j.chemgeo.2007.01.014.

Rae, A. S., Edmonds, M., Maclennan, J., Morgan, D., Houghton, B., Hartley, M. E. & Sides, I. (2016). Time scales of magma transport and mixing at Kīlauea volcano, Hawai'i. *Geology* **44**(6), 463–466. https://doi.org/10.1130/G37800.1.

Rasmussen, D. J., Plank, T. A., Roman, D. C., Power, J. A., Bodnar, R. J. & Hauri, E. H. (2018). When does eruption run-up begin? Multidisciplinary insight from the 1999 eruption of Shishaldin volcano. *Earth and Planetary Science Letters* **486**, 1–14. https://doi.org/10.1016/j.epsl.2018.01.001.

Read, P. B. (1979). *Geology, Meager Creek Geothermal Area, British Columbia*. Open File Report 603, Geological Survey of Canada, doi:https://doi.org/10.4095/129507

Read, P. B. (1990). Mount Meager complex, Garibaldi Belt, southwestern British Columbia. *Geoscience Canada* **17**(3), 167–170. https://journals.lib.unb.ca/index.php/GC/article/view/3672.

Reed, S. J. B. (2005) *Electron Microprobe Analysis and Scanning Electron Microscopy in Geology*. Cambridge University Press.

Rhodes, J., Dungan, M., Blanchard, D. & Long, P. (1979). Magma mixing at mid-ocean ridges: evidence from basalts drilled near 22°N on the mid-Atlantic ridge. *Tectonophysics* **55**(1–2), 35–61. https://doi.org/10.1016/0040-1951(79)90334-2.

Roeder, P. & Emslie, R. (1970). Olivine-liquid equilibrium. *Contributions to Mineralogy and Petrology* **29**(4), 275–289. https://doi.org/10.1007/BF00371276.

Rotheram-Clarke, D., Kelman, M., Ackerley, N., Le Moigne, Y., and Sond, M. (2023). The Government of Canada's first operational InSAR based volcano monitoring system. In *ESA Fringe 2023 Conference. European Space Agency (ESA), Abstract ID 166*, https://fringe2023.esa.int/agenda/

Ruth, D. C., Costa, F., Bouvet de Maisonneuve, C., Franco, L., Cortés, J. A. & Calder, E. S. (2018). Crystal and melt inclusion timescales reveal the evolution of magma migration before eruption. *Nature Communications* **9**(1), 2657. https://doi.org/10.1038/s41467-018-05086-8.

Schneider, C. A., Rasband, W. S. & Eliceiri, K. W. (2012). NIH image to image J: 25 years of image analysis. *Nature Methods* **9**(7), 671–675. https://doi.org/10.1038/nmeth.2089.

Shea, T., Costa, F., Krimer, D. & Hammer, J. E. (2015). Accuracy of timescales retrieved from diffusion modeling in olivine: a 3D perspective. *American Mineralogist* **100**(10), 2026–2042. https://doi.org/10.2138/am-2015-5163.

Stasiuk, M. V., Russell, J. K. & Hickson, C. J. (1996). Distribution, nature, and origins of the 2400 BP eruption products of Mount Meager, British Columbia: linkages between magma chemistry and eruption behaviour. *Bulletin of the Geological Survey of Canada* . https://doi.org/10.4095/208165.

Statistics Canada (2023). Census Profile. *2021 Census of Population. Statistics Canada Catalogue no. 98–316-X2021001, Ottawa. Released* November 15, 2023. (accessed September 20, 2025)

Thornber, C. R. & Huebner, J. S. (1985). Dissolution of olivine in basaltic liquids: experimental observations and applications. *American Mineralogist* **70**(9–10), 934–945.

Toplis, M. (2005). The thermodynamics of iron and magnesium partitioning between olivine and liquid: criteria for assessing and predicting equilibrium in natural and experimental systems. *Contributions to Mineralogy and Petrology* **149**, 22–39. https://doi.org/10.1007/s00410-004-0629-4.

Unnsteinsson, T., Flowers, G. & Williams-Jones, G. (2024). Formation and persistence of glaciovolcanic voids explored with analytical and numerical models. *Journal of Glaciology* **70**, 1–15. https://doi.org/10.1017/jog.2024.8.

Venugopal, S., Moune, S., Williams-Jones, G., Druitt, T., Vigouroux, N., Wilson, A. & Russell, J. K. (2020). Two distinct mantle sources beneath the Garibaldi Volcanic Belt: insight from olivine-hosted melt inclusions. *Chemical Geology* **532**, 119346. https://doi.org/10.1016/j.chemgeo.2019.119346.

Warwick, R., Williams-Jones, G., Kelman, M. & Witter, J. (2022). A scenario-based volcanic hazard assessment for the Mount Meager volcanic complex, *British Columbia. Journal of Applied Volcanology* **11**(1), 5. https://doi.org/10.1186/s13617-022-00114-1.

Welsch, B., Hammer, J. & Hellebrand, E. (2014). Phosphorus zoning reveals dendritic architecture of olivine. *Geology* **42**(10), 867–870. https://doi.org/10.1130/G35691.1.

Wieser, P. E., Kent, A. J., Till, C. B. & Abers, G. A. (2023). Geophysical and geochemical constraints on magma storage depths along the Cascade arc: knowns and unknowns. *Geochemistry, Geophysics, Geosystems* **24**(11). https://doi.org/10.1029/2023GC011025.

Wieser, P., Petrelli, M., Lubbers, J., Wieser, E., Özaydin, S., Kent, A. J. & Till, C. (2022). Thermobar: an open-source Python3 tool for thermobarometry and hygrometry. *Volcanica* **5**(2), 349–384. https://doi.org/10.30909/vol.05.02.349384.

Wilson, A. M. & Russell, J. K. (2017). Lillooet Glacier basalts, southwestern British Columbia, Canada: products of Quaternary glaciovolcanism. *Canadian Journal of Earth Sciences* **54**(6), 639–653. https://doi.org/10.1139/cjes-2016-0201.

Wilson, A. M. & Russell, J. K. (2019) Quaternary glaciovolcanism in the Canadian Cascade volcanic arc—Paleoenvironmental implications. In: Poland M., Garcia M., Camp V. & Grunder A. (eds) *Field Volcanology: A Tribute to the Distinguished Career of Don Swanson*. Geological Society of America, pp. 133–157.

Wilson, A. & Russell, J. (2020). Glacial pumping of a magma-charged lithosphere: a model for glaciovolcanic causality in magmatic arcs. *Earth and Planetary Science Letters* **548**, 116500. https://doi.org/10.1016/j.epsl.2020.116500.

Yoder, E. (2024). *Eruption Initiation Mechanisms and Timescales at a Very-High-Threat Washington Volcano: Clues from Crystal Cargo in Lavas from Mount Baker (Koma Kulshan)*. Master's Thesis, Central Washington University, https://digitalcommons.cwu.edu/etd/1943

Journal of Petrology, 2026, **67**, egag009
https://doi.org/10.1093/petrology/egag009
Original Manuscript